

From Hard Spheres and Cubes to Nonequilibrium Maps with Thirty-Some Years of Thermostatted Molecular Dynamics.

William Graham Hoover with Carol Griswold Hoover

Ruby Valley Research Institute

Highway Contract 60, Box 601

Ruby Valley, Nevada 89833

(Dated: August 18, 2020)

Abstract

This is our current research perspective on models providing insight into statistical mechanics. It is necessarily personal, emphasizing our own interest in simulation as it developed from the National Laboratories' work to the worldwide explosion of computation of today. We contrast the past and present in atomistic simulations, emphasizing those simple models which best achieve reproducibility and promote understanding. Few-body models with pair forces have led to today's "realistic" simulations with billions of atoms and molecules. Rapid advances in computer technology have led to change. Theoretical formalisms have largely been replaced by simulations incorporating ingenious algorithm development. We choose to study particularly simple, yet relevant, models directed toward understanding general principles. Simplicity remains a worthy goal, as does relevance. We discuss hard-particle virial series, melting, thermostatted oscillators with and without heat conduction, chaotic dynamics, fractals, the connection of Lyapunov spectra to thermodynamics, and finally simple linear maps. Along the way we mention directions in which additional modelling could provide more clarity and yet more interesting developments in the future.

Keywords: Statistical Physics, Reversibility, Nonequilibrium, Maps, Information Dimension D_I and D_{KY}

I. HOW THIS PROJECT BEGAN

This project began with the loss of a long-time colleague and good friend, Francis Hayin Ree, a generous and productive gentleman-scholar. As Bill's nine joint publications with Francis had appeared in the Journal of Chemical Physics from 1963 to 1968, Bill thought JCP well-suited to a short publication honoring Francis' memory and work. He wrote and submitted a memorial piece and soon received two pieces of news from JCP: The bad news: Memorial Articles were not allowed; The good news: a "Perspective" article touching on Francis' and our own joint work would be welcomed by the journal. Bill's original Memorial article was promptly published in Computational Methods in Science and Technology³⁹. We then set to work on this Perspective article just as the 2019 Chinese coronavirus arrived and became established in the United States, providing us with plenty of time at home in Ruby Valley, for contemplation, research, and writing.

A certain amount of "Perspective" is a natural side effect of being part of the research scene for 60 years. There is plenty of opportunity to distinguish useful from useless work and to reflect upon the difference. Two things stand out, with a third lurking in the background. First of all useful work is reproducible. In fact the reproduction of science is in itself extremely satisfying. Being able to follow a trail gives one confidence in blazing his own, leaving sufficient clues so that his fellows can follow suit. A second characteristic of useful work is simplicity as recommended by Occam and Thoreau. Simplicity saves time in the assessment and reproduction and generalization and also indicates a kind regard for one's fellows. When Bill read Zwanzig's claim that cubes could bound results for spheres⁷⁶ it was relatively easy to see that the "bound" was mistaken, as Zwanzig's ideas were expressed clearly. When Bill read Nosé's discussion of canonical dynamics^{50,51} he entered into a struggle to understand ideas which were more formal than useful and though stimulating, were in the end too complex in their presentation. Simplicity through the exploration of simple models is the key to understanding and utility.

By studying the simple harmonic oscillator²⁴ Bill began to see not only the limited usefulness of Nosé's original work but also the compelling vision which had motivated him. Simplicity can steer us toward a third research benefit, modular thinking and working, making the repeated use of integrators, graphics, text software, and the underlying ideas that motivated their development. It is a cliché that simplicity can be carried too far.

Keeping up with the literature is certainly useful, and nearly essential. At the frontier this involves realtime communication with those who are generating the work. It would be very useful if those journals which are not free to read would sunset their prohibitions after a reasonable time (a year or two ?) so that those without access to institutional accounts or libraries could more easily contribute to the research effort.

II. HARD-PARTICLE LEGACIES OF GIBBS, TONKS, AND THE MAYERS

A. Becoming Familiar with Willard Gibbs' Statistical Mechanics

Bill's scientific journey began with Chemistry from Louise "Quiz" Stull at Washington's Woodrow Wilson High, and continued with Physical Chemistry from Luke Steiner at Oberlin College, with a mix of Gibbs' Statistical Mechanics and kinetic theory from Stuart Rice at MIT and from Bill's thesis advisor, Andy De Rocco at the University of Michigan. This necessary, welcome, and exciting scientific groundwork was topped off by George Uhlenbeck's Boltzmann Equation course at Ann Arbor. Finally Bill was up-to-speed as a Chemical Physics graduate student, vintage 1958-1961. The John Kirkwood Memorial issue of the Journal of Chemical Physics (November 1960) and the Mayers' 1940 *Statistical Mechanics* text were required reading at that time. The Mayers' work was concentrated on the virial expansion of the compressibility factor in powers of the number density $\rho \equiv (N/V)$,

$$\frac{PV}{NkT} = 1 + B_2\rho^1 + B_3\rho^2 + B_4\rho^3 + B_5\rho^4 + B_6\rho^5 + B_7\rho^6 + \dots .$$

Exactly these same coefficients represent the focus of Gibbs' work, his canonical partition function $Z(N, V, T) = e^{-A/kT}$, where $A(N, V, T)$ is Helmholtz' free energy :

$$\ln\left(\left[\frac{Z(N,V,T)}{Z_{\text{ideal}}(N,V,T)}\right]^{1/N}\right) = -B_2\rho^1 - \frac{1}{2}B_3\rho^2 - \frac{1}{3}B_4\rho^3 - \frac{1}{4}B_5\rho^4 - \frac{1}{5}B_6\rho^5 - \frac{1}{6}B_7\rho^6 - \dots .$$

Andy De Rocco assured his class "If you know Z you know everything!" Here "everything" includes the two derivatives of the free energy, pressure and entropy: $dA = -PdV - SdT$. Evidently on the way to knowing everything, the evaluation of virial coefficients $\{ B_n \}$, was worth pursuing. Bill found that Lewi Tonks' 1936 work served as a good introduction.

B. Lewi Tonks' Hard Rod Model for Fluids and Solids

In 1936, prior to the Mayers' work, Lewi Tonks had worked out the pressure-volume-temperature equation of state for hard rods of unit length⁶⁶, the one-dimensional analog of hard spheres:

$$\frac{PV}{NkT} = 1/(1 - \rho) = 1 + \rho + \rho^2 + \rho^3 + \rho^4 + \rho^5 + \rho^6 + \dots$$

This benchmark equation continues to provide useful checks on computational virial-series work for fluids. It also serves as an introduction to the free-volume model of the solid phase²¹. If we imagine an equally-spaced system of hard rods of unit length then each of them can move a distance $(V/N) - 1$ to the left or to the right, giving a “free volume” estimate of the space accessible to a typical particle, $v_f = 2(V/N) - 2$. For hard parallel squares and cubes an analogous approximation, using the square and simple cubic lattice structures, gives:

$$\sqrt[2]{v_f} = 2(\sqrt[2]{V/N} - 1) \text{ [squares] } ; \sqrt[3]{v_f} = 2(\sqrt[3]{V/N} - 1) \text{ [cubes] } .$$

The corresponding values of the pressure constitute the “free-volume” equation of state for the “compressibility factor” $PV/NkT \equiv Z$ for hard rods, squares, and cubes:

$$Z = (1 - \sqrt[2]{\rho})^{-1} \text{ [Rods] } ; Z = (1 - \sqrt[2]{\rho})^{-1} \text{ [Squares] } ; Z = (1 - \sqrt[3]{\rho})^{-1} \text{ [Cubes] } .$$

Finite systems of squares⁶⁰ and cubes have been shown to follow this equation of state precisely at high density¹⁹.

The analogous approximations for solid-phase disks and spheres agree with computer simulations with deviations of the order of unity. Tonks' hard rod model and his paper with its exaggerated title, “The Complete Equation of State of One, Two and Three-Dimensional Gases of Hard Elastic Spheres”, served as a prototype for both kinds of hard-particle phases, the fluid and the solid. In order to go beyond Tonks' approximate ideas it is necessary to adopt the Mayers' contribution to statistical mechanics so as to understand the “star graphs” necessary to the computation of the virial coefficients beyond the four known in the precomputer days.

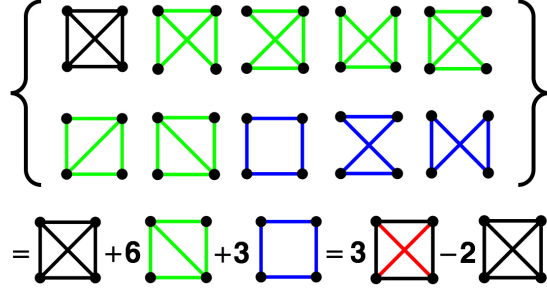


FIG. 1: The three types of four-point “star graphs” are shown above between braces, $\{\dots\}$. The bottom row indicates that the ten summed-up integrals can be reexpressed in terms of the “complete star” integral, with six f -function links together with a “Ree-Hoover” integral with four f functions and two Boltzmann-factor links (shown in red). For drawings of the star graphs with up to seven points see reference 18.

C. The Mayers’ Star Graphs

The Mayers showed that the n th virial coefficient can be written as a sum of integrals represented by n -particle “star graphs”. The ten four-point star graphs contributing to B_4 are shown in **figure 1**. At Bill’s *Alma Mater* of 1958-1961, the University of Michigan, George Ford and George Uhlenbeck had recently generated a list of all the topologically distinct types of star graphs up to, and including, the 468 7-point star graphs contributing to B_7 , the seventh term in the virial series¹⁸. For $n > 2$ any n -point star graph has at least two independent paths linking any pair of points in the graph. The simplest star, the “ring” star graph has n links while the “complete star” graph has the maximum number of links, $n(n - 1)/2$. Each link, or bond, or edge represents a corresponding Mayer “f-bond” in an n -body integral. The Mayer f represents $e^{-\phi/kT} - 1$, where ϕ is the pair potential, and so is equal to either zero or minus one for “hard particles”. Finally each virial coefficient is proportional to the summed-up configurational integrals of all these star graphs.

D. Calculating Virial Coefficients for Squares and Cubes at Michigan

At Michigan, Bill’s 1960-1961 thesis work on the virial series for squares and cubes was motivated by an incautious remark of Bob Zwanzig in the 1956 *Journal of Chemical Physics*⁷⁶:

“Upper and lower bounds on the virial coefficients of gases composed of rigid

circles or rigid spheres are obtained in terms of the virial coefficients for the parallel squares and parallel cubes.”

To investigate this claim Bill set about generalizing Tonks’ hard-rod work to parallel hard squares and cubes, using the Michigan Algorithmic Decoder “MAD” programming language, much like today’s FORTRAN.

The n th virial coefficient was expressed by the Mayers as the sum of all the n -point star-graph integrals of the type shown for $n = 4$ in **figure 1**. Of the 64 4-point graphs only ten contribute to the virial coefficient B_4 . The other 54 four-point graphs do not. The number of topologically distinct types of star graphs, one three-point graph, three four-point types, 10 five-point, 56 six-point, and 468 seven-point types rapidly approaches $2^{n(n-1)/2}/n!$ for large n . The n or more bonds holding the points of the graph together represent Mayer f functions, $e^{-\phi/kT} - 1$ where ϕ is the pair potential, k is Boltzmann’s constant, and T is the temperature.

E. Virial Coefficients Using Ree-Hoover Graphs⁵⁹

figure 1 showed the Mayers’ ten four-point star graphs in the top two rows. Combining those with identical integrals, identified by using the same color for the links, gives the first three entries in the bottom row. Those three types of four-particle integrals are reduced to just two Ree-Hoover graphs by introducing the identity $1 \equiv e^{-\phi/kT} - f$. The Mayers’ f functions, $\{ e^{-\phi/kT} - 1 \}$ correspond to all of the black, blue, and green lines in the figure. The Boltzmann factors used in the Ree-Hoover graph representation of the integrals (at bottom right) are the two links shown in red. Of all the Ree-Hoover graphs only the complete-star integral, with its $n(n - 1)/2$ f -links, is nonzero when applied to Tonks’ hard-rod problem.

The integrals corresponding to the graphs can be evaluated numerically, but there are so many of them that the enumeration is instead the most time-consuming aspect of the computations. For hard cubes or spheres or parallel squares and disks the integrands are all ± 1 whenever linked particles overlap, and zero otherwise. Bill was able to program the evaluation of all the integral types for squares and cubes, including up to seven points. Summing the star integrals he soon found that both B_6 and B_7 were negative for hard cubes¹⁸. This was quite a surprise, as hard-particle collisions necessarily make only positive contributions to the pressure. Because both B_6 and B_7 were thought to be positive for hard

spheres (as Francis Ree and Bill confirmed precisely in 1966), these discrepancies implied that Zwanzig was wrong. A quick phonecall from Andy De Rocco in Ann Arbor to Bob Zwanzig in College Park confirmed this conclusion, certainly a “rare event”, exciting for a youngish graduate student to discover. It was time for Bill to write his thesis, completed in August 1961.

F. Calculating Virial Coefficients for Disks and Spheres at Livermore

After a post-doctoral year working on integral equations and their approximate virial series at Duke, Bill was hired at the Lawrence Radiation Laboratory by Berni Alder and soon began working closely with a contemporary researcher from Korea, Francis Hayin Ree. Both Berni and Edward Teller provided support for this work. Francis and Bill introduced “Ree-Hoover” graphs in a reformulation of the Mayer’s work⁵⁹. By introducing $e^{-\phi/kT}$ links as well as $f = e^{-\phi/kT} - 1$ links into the star graphs, they reformulated the Mayer’s expressions, reducing the 468 seven-point star integrals to 171 simpler ones, each with 21 links of the two different types, f and $e^{-\phi/kT}$. As shown in detail in **figure 1** the fourth virial coefficient requires only two integral types rather than three, one with 6 f s, the other with four f s and two $e^{-\phi/kT}$ links. Francis and Bill were able to evaluate the integrals giving B_6 and B_7 for disks and spheres in 1968²⁰. They were able to estimate the densities and pressure of the hard-disk and hard-sphere melting and freezing transitions by Padé-approximant extrapolation.

G. Modern Calculations of Virial Coefficients

Some 40 years later Nathan Clisby and Barry McCoy used the Ree-Hoover idea to pursue the eighth, ninth, and tenth coefficients for multi-dimensional hard spheres⁹, and found that the 9,743,542 ten-point Mayer f graphs could be expressed in terms of just 4,980,756 “Ree-Hoover” graphs with two kinds of links, f and $e^{-\phi/kT}$. Clisby and McCoy discovered that all the virial coefficients through the tenth are positive for one, two, three, and four-dimensional hard spheres but that the fourth coefficient becomes negative for the first time for eight-dimensional spheres, hard particles whose cartesian description requires eight orthogonal directions in eight-dimensional space rather than the simpler two dimensions of disks and

three of cubes. The sign change is easily understood, in retrospect. As dimensionality increases the n -link ring integral comes to dominate each exponent. For hard particles, with all the ring-integral f links negative, (-1) , this causes the virial coefficients after B_2 to alternate in sign, with B_4, B_6, B_8, \dots necessarily negative and B_3, B_5, \dots positive, as indicated in Clisby and McCoy's work.

In seven more years Richard Wheatley evaluated the eleventh and twelfth coefficients for three-dimensional hard spheres⁷⁰. At the freezing density, about two-thirds of close packing, the hard-sphere compressibility factor is about 12.5. The 12-term virial series sum at that density is 12.39. Of all the statistical-mechanical topics which we have studied over the past sixty years the virial series, for both hard-particle and "realistic" models, has progressed the most⁷¹. In 2014, Zhang and Pettitt⁷⁵ published the first 64 coefficients in the series for multidimensional hyperspheres of as many as 100 dimensions!

We worked on two-dimensional squares and three-dimensional cubes with Marcus Bannerman in 2009. The three of us found that parallel squares likely have a second-order (discontinuity in slope) phase transition at a density near 0.793 and that cubes behave even more smoothly. So far these results have no theoretical explanation, though they are well established from the numerical standpoint. Wheatley's valuable contributions suggest that for hard squares and cubes the truncated virial series is as reasonable a choice as the approximants. For both squares and cubes the discrepancies between the truncated and Padé equations of state increased with the additional knowledge of B_8 and B_9 .

The number and complexity of the star graphs limited the number of computationally feasible terms to seven in 1961. By 2013 that number had increased, from seven to twelve, through the efforts of Nathan Clisby, Barry McCoy, and Richard Wheatley^{9,70}.

Disks and spheres have already been thoroughly investigated. Now, in 2020, it is high time that the hard-cubes model be reinvestigated, taking advantage of the tremendous computational progress in both hardware and algorithms made since 1961. The mechanism for the hard-disk melting transition was identified in 1962. That and the melting and freezing transitions' locations are the subjects of the following subsection.

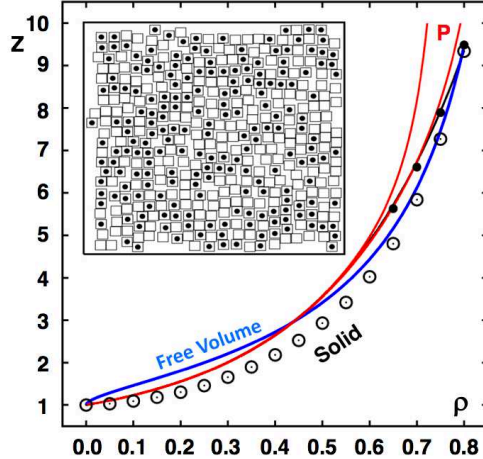


FIG. 2: Hard-square equations of state with the compressibility factor $Z = PV/NkT$ shown as a function of the density relative to close packing ρ . “Solid” data are from single-occupancy cell simulations, distinct from the free-volume solid-phase approximation, $(1 - \sqrt{\rho})^{-1}$, shown in blue. The four filled circles are from 1600-square simulations using 1000 collisions per particle. The two Padé approximants (right to left and shown in red) indicate the change from using seven virial coefficients to using nine. These two approximants are ratios of cubics and quartics in the density, respectively. The inset shows a typical configuration of 400 squares at $\rho = 2/3$ where the dotted particles originally occupied the even-numbered rows. Marcus Bannerman’s minute-long YouTube presentation of “Parallel Hard Cubes” is worth well more than a thousand words.

H. Padé Approximants, A Useful Extrapolation Tool?

The steady progress in finding virial coefficients suggests a program of extrapolation and checking, much like the economists’ and climate scientists’ efforts to understand a country’s financial and environmental futures. For virial coefficients a systematic nineteenth-century extrapolation procedure, used by Henri Padé and Georg Frobenius, can be used to generate predicted sums of the entire virial series. Here is an example Padé approximation, extending the truncated five-term virial series for hard parallel squares to a closed form, a ratio of quadratics in the density.

$$\frac{PV}{NkT} \simeq \frac{1 + N_1\rho + N_2\rho^2}{1 + D_1\rho + D_2\rho^2} \simeq 1 + B_2\rho + B_3\rho^2 + B_4\rho^3 + B_5\rho^4 ,$$

the unknowns in the numerator $\{ N_i \}$ and denominator $\{ D_i \}$ can be evaluated by equating coefficients of like powers of the density. The resulting system of linear equations is then solved by matrix inversion. The four coefficients B_2 through B_5 are enough information to

identify two unknowns each in the numerator and denominator:

$$\begin{pmatrix} 1 & 0 & -1 & 0 \\ 0 & 1 & -B_2 & -1 \\ 0 & 0 & -B_3 & -B_2 \\ 0 & 0 & -B_4 & -B_3 \end{pmatrix} \begin{pmatrix} N_1 \\ N_2 \\ D_1 \\ D_2 \end{pmatrix} = \begin{pmatrix} B_2 \\ B_3 \\ B_4 \\ B_5 \end{pmatrix} .$$

The solution of this example problem is :

$$\frac{1.000000 - 0.133335\rho + 0.099999\rho^2}{1.000000 - 2.133335\rho + 1.366669\rho^2} \simeq 1 + B_2\rho + B_3\rho^2 + B_4\rho^3 + B_5\rho^4 .$$

For hard parallel squares Hoover and DeRocco found the following results (rounded to six figures after the decimal point):

$$\{ B_2 = +2.000000 ; B_3 = +3.000000 ; B_4 = +3.666667 \} ;$$

$$\{ B_5 = +3.722222 ; B_6 = +3.025000 ; B_7 = +1.650648 \} .$$

For cubes they found:

$$\{ B_2 = +4.000000 ; B_3 = +9.000000 ; B_4 = +11.333333 \} ;$$

$$\{ B_5 = +3.159722 ; B_6 = -18.879630 ; B_7 = -43.505432 \} .$$

In 2020 Wheatley reconsidered the parallel square and cube systems, finding that both B_8 and B_9 are negative for squares, the first negative exponents found for that system. The exponents for cubes continue to be much larger, indicating a much less useful series in three dimensions than in two :

$$\{ B_8 = -0.04094 ; B_9 = -1.4125 ; B_{10} = -1.710 \}_{\text{squares}} ;$$

$$\{ B_8 = -37.3010 ; B_9 = +40.8927 ; B_{10} = +171.5 \}_{\text{cubes}} .$$

Cell models describing the motion of a single particle in the fixed field of its neighbors are not just crude approximations of reality. For hard particles one can imagine a very light specimen in a system sampling its cell while its fellows scarcely move. It is evident that this picture can be made exact and it would be an excellent thesis project to make this concept rigorous. For more details see the discussion of hard-disk free volumes in subsection II.k.

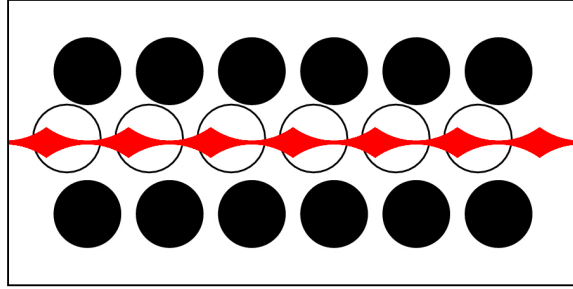


FIG. 3: The correlated cell model³ describes the (red) free volume available to a row of moving (white) disks constrained by fixed (black) disks in neighboring rows. At a density three fourths of the close-packed the free volumes join up, as shown here, and allow “hexatic” sliding, causing a van der Waals loop in the equation of state.

I. Melting/Freezing, *via* the Correlated Cell Model

In the 1950s Berni Alder and Tom Wainwright developed hard-sphere and square-well molecular dynamics at Livermore² while Bill Wood and Jack Jacobson implemented Metropolis’ Monte Carlo algorithm at Los Alamos⁷², with the two groups cooperating closely and comparing their results. The existence of a sharp fluid/solid transition was still controversial in 1957. In January, at a meeting at the Stevens Institute George Uhlenbeck requested a show-of-hands on the question of belief or disbelief in a “transition point” for hard spheres. According to the record⁵⁴ he announced the verdict, “Even, again!”, recalling a Seattle vote on the same question the previous Fall. By mid-August 1957 the existence of a first-order solid-fluid transition was “strongly suggested” by Wood and Jacobson⁷² and “strongly indicated” by Alder and Wainwright¹ in their near-simultaneous cooperative publications. Memories of this valuable four-man collaboration evidently faded somewhat over time^{5,74}.

J. The Hard-Disk Hexatic Phase

The situation was then a bit less clear for disks than for spheres. Disks are well understood today¹¹. Disks exhibit a “hexatic” phase prior to melting, a modification of the usual solid with cooperative motion parallel to the three sets of close-packed rows of particles. Wood remarked on a circular “ring-around-the-rosey” cooperative motion of disks in his voluminous 1963 Los Alamos report⁷³. By then Alder and Wainwright’s movies had shown row-wise

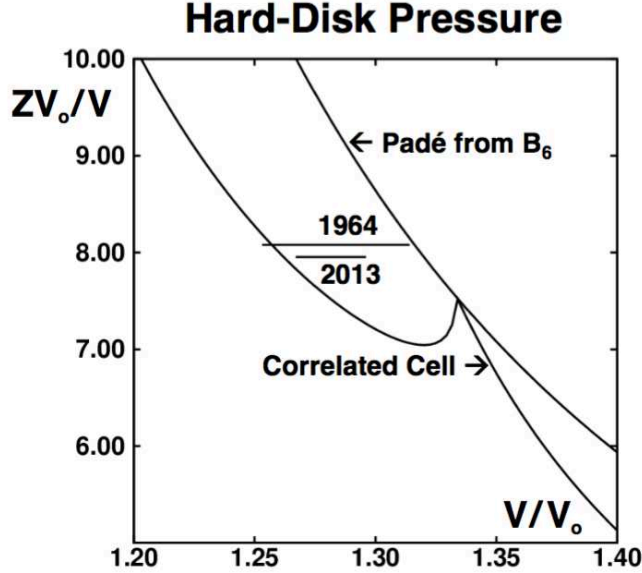


FIG. 4: Here we show approximations to PV_o/NkT for hard disks, where V_o is the close-packed volume. A Padé approximant to the excess entropy, as the ratio of two quadratics in density, given in reference 19, was used to estimate the 1964 fluid-solid tie-line pressure. The accurate 2013 simulations’ tie-line pressure comes from reference 11, using 2^{20} disks. The single-disk correlated cell model prediction from reference 3 is surprisingly good. See also reference 4.

hexatic motion as a precursor to melting. They and Bill developed a simple “correlated cell model” incorporating the row-wise motion in a two-disk periodic cell. See **figures 3 and 4**. The periodic boundary condition provides a geometry equivalent to the motion of two infinitely-long parallel rows of disks. With one of the two particle rows fixed the free area integral, $a_f = [\int \int e^{-\phi/kT} dx dy]_{\text{cell}}$, available to the other one is:

$$a_f = \sqrt{3}D^2 - \frac{1}{2}\sqrt{4D^2 - D^4} - 2 \arcsin(\sqrt{D^2/4}) .$$

Here $D > 1$ is the center-to-center separation of the unit-diameter disks in the perfect lattice. The disk number density, relative to close-packing is D^{-2} . At densities greater than three-fourths of the closest-packed the sliding motion is prevented and there are two additional terms:

$$\delta a_f = -\frac{1}{2}\sqrt{12D^2 - 9D^4} + 2 \arccos(\sqrt{3D^2/4}) .$$

The equation of state for this “correlated cell model” follows easily from a numerical differentiation of the free area a_f , $\frac{PV}{NkT} = 1 + [d \ln(a_f)/d \ln(D^2)]$. See **figure 4**.

That the sliding mechanism of the correlated-cell model is reflected in the equation of state can be seen in the good agreement of the transition pressure with that measured by

a variety of numerical methods. Now, more than half a century after Alder, Jacobson, Wainwright, and Wood’s work, with from 12 to 870 particles, the hard-disk and hard-sphere transitions have been thoroughly investigated^{11,40}. Many algorithms were implemented and compared for system sizes up to 2^{20} particles, corresponding to system widths of about 1000 disks and 100 spheres.

K. Single-Speed Molecular Dynamics for Squares and Cubes

Although Zwanzig’s hard parallel square and cube models were slower to be understood, the simplicity of their Cartesian collisions suggested useful algorithms for disks and spheres. In 2009 Marcus Bannerman invented and implemented a special square and cube dynamics in which every particle’s Cartesian velocity components were ± 1 . Collisions left the overall velocity distribution unchanged³². This same idea, reminiscent of the Ehrenfests’ “Wind-Tree” model, can be, and has been, applied to disks and spheres. By 2015 Krauth and his several coworkers had applied a similar mock dynamics to their Monte Carlo simulations¹¹. Displacement moves of single disks and spheres were made in the two or three Cartesian directions, with each move terminating in a mock Cartesian collision. Just as in the hard parallel simulations these successive displacements could be continued in Cartesian fashion without altering the longtime-averaged configurational distribution needed to determine the pressure. This mock collision method has the advantage of determining a collision rate directly without the need for extrapolating binning data to find the probability density of colliding particles.

In addition to the mechanical pressure-volume diagnosis of melting it is feasible, and certainly equally convincing, to locate transitions by estimating the entropies of the coexisting phases. This approach was undertaken by Bill and Francis Ree in 1968²⁰. The resulting estimates of the transition pressures were $PV_o/NkT = 8.08$ for disks and 8.27 for spheres, where the close-packed volumes V_o/N are $\sqrt{3/4}$ and $\sqrt{1/2}$ for particles of unit diameter. This approach was also applied to parallel square and cubes by Bannerman in 2009, but the relative weakness of the transitions in those two cases precluded definite results.

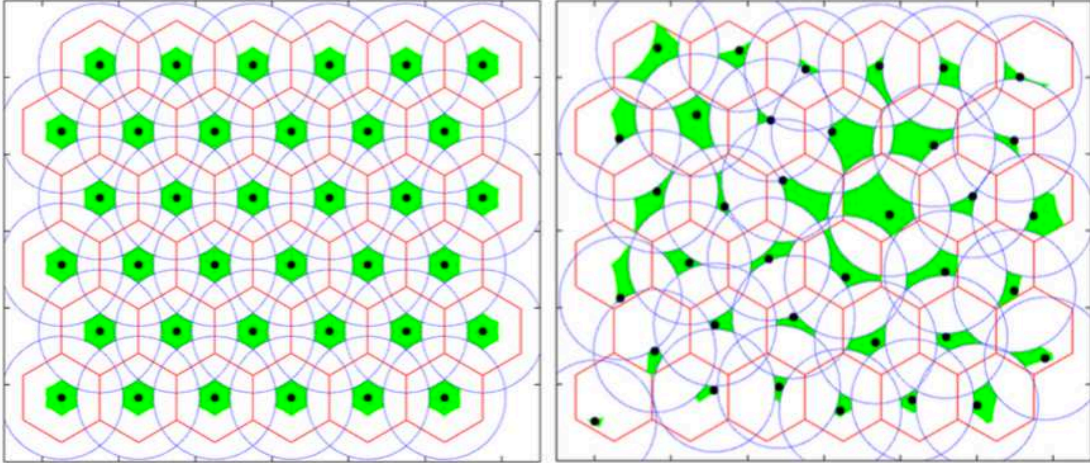


FIG. 5: Hard-disk free volumes with periodic boundary conditions from a Monte Carlo simulation at a density of 0.64 relative to close packing. The volume accessible to each disk with the others held fixed, is shown in green. The initial perfect lattice is shown to the left and a typical fluid configuration appears at the right. The exclusion disks drawn around each particle have a radius equal to the disk diameter.

L. Communal Entropy, Hard-Particle Free Volumes

Prior to the computer simulations of the middle 1950s theoretical understanding of many-body systems was restricted to the Mayers’ virial series and a variety of approximate models, of which the “cell model” was particularly physical. The configurational states available to fluid or solid particles were estimated by models of a typical particle’s surroundings. See **figure 5** for a modern computational realization of this idea for 36 hard disks. Particle motions are restricted both by cell boundaries, enclosing volumes of (V/N) each, as well as by their interactions with neighboring particles. To the left we see free volumes available to hard disks in a perfect solid structure. These approximate the N th root of the configurational partition function. Numerical work shows that the N th root is somewhat larger. To the right a Monte Carlo configuration at the same overall density, 0.64 relative to the close-packed density, provides a distribution of free volumes, each of them corresponding to the instantaneous states accessible to a light particle confined by its heavier neighbors.

The cell picture has a defect at low density, predicting a configurational phase volume smaller than Gibbs’ by a factor e^N . In 1950, Kirkwood formalized the idea of a “communal” entropy as an explanation of the extra factor of $e = 2.71828$ in the ideal-gas configurational

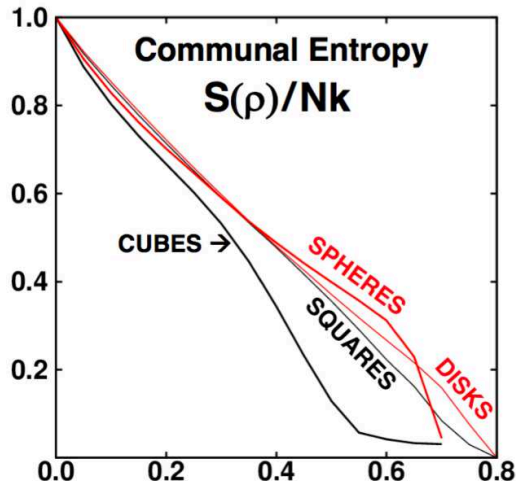


FIG. 6: Density dependence of the fluid’s entropy relative to the single-occupancy entropy, Kirkwood’s “communal entropy” $S_C \equiv S_{\text{Fluid}} - S_{\text{SO}}$, for four hard-particle systems^{4,20,32}. Presently neither squares nor cubes are thought to exhibit a first-order freezing transition although Marcus Bannerman is currently reinvestigating this question.

integral⁴³.

$$(1/N!) \prod_{i=1}^N [\int_0^v dr_i] = \lim_{N \rightarrow \infty} [(V^N)/N!] \simeq (Ve/N)^N = (ev_f)^N .$$

The division of the N -particle integral V^N by $N!$ accounts for the indistinguishability of the N identical particles. We see in **figure 6** that Kirkwood’s communal entropy dies away slowly, nearly linearly in density, for hard squares, disks, cubes, and spheres.

M. Single-Occupancy Solid Entropy Calculation

Francis Ree and Bill adopted Kirkwood’s particle-in-cell notion to carry out a precise numerical evaluation of the solid-phase entropy^{4,20}. Because the velocity distributions of the solid and fluid are identical only the configurational entropy determines phase stability. Kirkwood’s idea of confining particles in cells provides a way to extend a “single-occupancy” cell model of the solid all the way from close-packing to zero density. For simplicity we consider two two-dimensional hard-particle models, hard disks and hard parallel squares.

By confining (the center of) every particle in a manybody system of hard disks or squares to its own hexagonal or square cell of area (V/N) , and integrating the resulting pressure from low density into the solid phase, the vacancy-free solid’s entropy, relative to that of an

ideal gas at the same density and temperature, can be determined with an uncertainty of order $0.01Nk$, where k is Boltzmann’s constant:

$$(S_{\text{ideal}} - S)/Nk = 1 + \int_o^\rho \left[\frac{PV}{NkT} - 1 \right] d \ln(\rho') .$$

We used this approach to determine the coexisting densities for disks (0.761 and 0.798) and spheres (0.667 and 0.736) relative to close-packing. For squares the transition density we determined with Marcus Bannerman in 2009 is 0.793, nearly the same as the melting density for hard disks. For cubes the number dependence is so large, including many apparent changes in the sign of the $P(\rho)$ curvature, that no definite phase-transition density was apparent! Certainly this is a problem that will eventually be solved through the inexorable exponential advances in computational capabilities summarized by Moore’s Law. With new algorithms additional virial coefficients and compressibility data for squares and cubes would be a good investment of computer time. The entropies of simple cubic and brick-wall-structured three-dimensional crystals are also reasonable and readily accessible research goals. The entropy associated with solid-phase vacancies is also readily accessible⁶⁴.

Bob Zwanzig pointed out that, apart from sign, the Mayer’s star integrals in two or three dimensions are just the squares and cubes of the corresponding one-dimensional hard-rod integrals⁷⁶. Additionally, the independence of the spatial distribution to the velocity distribution means that the molecular dynamics of squares and cubes can be replaced by the simpler one with the speeds of all particles made identical by choosing each of the Cartesian velocity components equal to ± 1 .

Although treating squares and cubes is relatively simple from the conceptual and computational standpoints, numerical work reveals considerable complexity. For example, squares have a smooth equation of state without any apparent jumps in density as a function of pressure. There does appear to be a transition between two distinct phases (fluid and solid), a weak “second-order” one, corresponding to a discontinuity in slope rather than magnitude. The situation with respect to cubes is worse. For “reasonable” system sizes such as 10^5 particles, $P(\rho)$ exhibits curvature irregularities quite unlike the smooth regular nature of the hard-sphere equation of state. The large-scale Monte Carlo simulations of 2013 and 2015 show clear van der Waals’ loops for disks and spheres^{11,40}. It would be a worthwhile project to follow the number-dependence of the pressure-volume loops and the entropy, along with additional virial coefficients, as guides to understanding the square and cube phase diagrams.

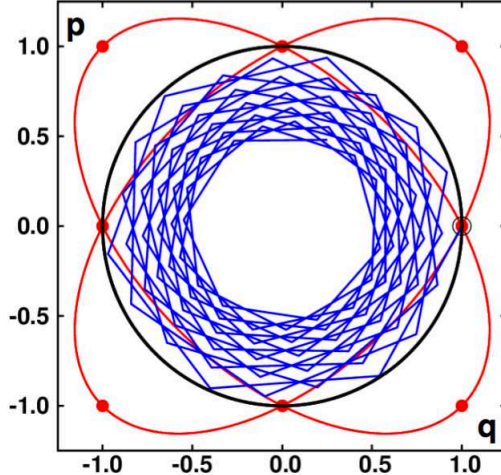


FIG. 7: Harmonic oscillator orbits with fourth-order Runge-Kutta $dt = 1$ (blue). Yoshida discovered a timestep-dependent Hamiltonian, $\mathcal{H}_Y = (q^2 \pm qpdt + p^2)/2$, which generates continuous trajectories that reproduce the Størmer-Verlet numerical solution. The common points are shown in red in **figure 7** for the special case $dt = 1$. The exact $dt = 0$ solution, $q^2 + p^2 = 1$, is shown in black with the initial point $(q, p) = (0, 1)$ emphasized.

A rigorous argument for the weighting of free volumes so as to calculate an average pressure could be a useful part of an interesting thesis.

With a firm grasp on the properties of hard-particle equilibrium systems let us turn next to methods appropriate to smooth continuous interparticle interactions, the solution of ordinary differential motion equations, both at and away from equilibrium.

III. HARMONIC-OSCILLATOR BASED MODELS

Molecular dynamics is the numerical solution of the particle equations of motion, often just Newton's equations for the motion of point masses, $\{ F = ma \}$. As acceleration $a = \dot{v} = \ddot{q}$ is the second time derivative of the coordinate, a centered second-difference approximation, with discrepancy $\frac{dt^2}{12} \ddot{\ddot{q}}$, can provide the needed algorithm for a numerical solution. This algorithm's many users have included Loup Verlet, Enrico Fermi, Carl Størmer, and Isaac Newton. The one-dimensional harmonic oscillator (with coordinate q and with both mass and force constant unity) is a useful test case⁶⁷. For the oscillator there is an analytic solution:

$$q(t + dt) = 2q(t) - q(t - dt) - dt^2 q(t) \rightarrow q \propto \cos(\omega t) .$$

Assume a periodic solution $q(t) \propto e^{i\omega t}$ and then divide by $2q(t)$. The result is :

$$\cos(\omega dt) = 1 - \frac{dt^2}{2}\omega^2 + \frac{dt^4}{24}\omega^4 - \dots = 1 - \frac{dt^2}{2} \rightarrow \omega = 1 + \frac{dt^2}{24} + \dots .$$

For the extreme example $dt = 1$, shown in **figure 7**, the approximate oscillator frequency is (1/6) revolution per unit of time. This exceeds the exact frequency $(1/2\pi)$ by a factor of $\pi/3 = 1.0472 \simeq 1 + \frac{1}{24} = 1.041\dot{6}$. Typical molecular dynamics timesteps are ten to one hundred times smaller than atomistic vibrational periods.

figure 7 shows the periodic six-point oscillator orbit using the finite-difference algorithm starting at $(q, p) = (1, 0)$. Also shown there is the continuous periodic solution of Yoshida's Hamiltonian with the finite-difference timestep set equal to unity :

$$\mathcal{H}_Y = (q^2 + qpdt + p^2)/2 \longrightarrow \{ \ddot{q} = -(3/4)q ; \ddot{p} = -(3/4)p \} .$$

Yoshida showed that the finite-difference solution differs from the exact $dt \rightarrow 0$ limit by a term of order dt . In the harmonic oscillator example there are no higher-order terms so that the agreement is exact.

The centered-second-difference Størmer-Verlet algorithm is perfectly satisfactory for systems obeying Newtonian or Hamiltonian mechanics, small or large so long as the boundaries and the energy are fixed. Simulations at specified values of temperature and pressure required new ideas. Shuichi Nosé furnished them in 1984.

A. Nosé's Route to Isothermal Nosé-Hoover Dynamics

In 1984 Shuichi Nosé took a giant step toward an ambitious goal, finding isothermal and isobaric modifications of Hamiltonian mechanics^{50,51}. We discuss the isothermal case here. Nosé wanted to reproduce Gibbs' canonical distribution with molecular dynamics. He discovered a Hamiltonian, containing what he called a "time-scaling" variable s and its conjugate momentum p_s . For simplicity, which is highly desirable in view of the complexity of Nosé's work, we confine our discussion here to the dynamics of a one-dimensional harmonic oscillator with mass, force constant, and relaxation time all equal to unity. In this case Nosé's novel Hamiltonian and the motion equations following from it, are

$$\mathcal{H}_N = (1/2)[(p/s)^2 + q^2 + p_s^2 + \ln(s^2)] \longrightarrow$$

$$\{ \dot{q} = (p/s^2) ; \dot{p} = -q ; \dot{s} = p_s ; \dot{p}_s = (p^2/s^3) - (1/s) \} .$$

Nosé observed that a logarithmic potential is uniquely capable of providing motion equations consistent with the canonical distribution. A constant Hamiltonian with the logarithmic potential implies $s \propto e^{-\mathcal{H}/kT}$, where Nosé termed his s the “time-scaling variable”.

Unfortunately his time-scaling approach encounters both verbal and computational complexities, with two sets of variables, “real” and “virtual”, exceptionally “stiff” motion equations (as s is often small), and two sets of timesteps. In Nosé’s words,

“The length of the timestep is unequal in the canonical ensemble molecular dynamics method” [due to the presence of the time-scaling variable s].

Though the idea of adding an additional thermostating variable is a good one there are two much simpler routes to Nosé’s goal. Let us reverse time in discussing them by first considering Dettmann’s approach, from July 1996¹⁰, as it is a greatly-simplified version of Nosé’s. We then take up Hoover’s even simpler one, from 1984²⁴, which approaches the canonical-ensemble goal directly, without the unnecessary distraction of Hamiltonian mechanics.

B. Dettmann’s Route to Nosé-Hoover Dynamics in 1996

Bill and Carl Dettmann discussed the need for a Hamiltonian approach to canonical dynamics during a CECAM meeting at Lyon. Carl discovered that a Hamiltonian similar to Nosé’s, when set equal to zero (!), is precisely consistent with the canonical distribution:

$$s\mathcal{H}_N = \mathcal{H}_D = (1/2)[(p^2/s) + sq^2 + sp_s^2 + s \ln(s^2)] \equiv 0 .$$

Choosing $\mathcal{H}_D = 0$ for the Hamiltonian’s value simplifies the time derivative of p_s as follows:

$$\{ \dot{q} = (p/s) ; \dot{p} = -sq ; \dot{s} = sp_s ; \dot{p}_s = (1/2)[(p/s)^2 - q^2 - p_s^2 - \ln(s^2) - 2] = (p/s)^2 - 1 \} .$$

Then we can either replace the combination (p/s) by p or equivalently \dot{q} . With the latter choice the equation of motion is just the usual Newtonian one with the addition of a time-reversible friction. Changing the signs of the velocity \dot{q} and friction coefficient ζ leaves the equations of motion unchanged, confirming reversibility. Any Nosé trajectory $q(t)$ can be

followed equally well forward or backward without change despite the “frictional” control forces.

$$\{ \ddot{q} = d(p/s)/dt = (\dot{p}/s) - (p/s)(\dot{s}/s) = -q - p_s \dot{q} \} \stackrel{\zeta=p_s}{\longleftrightarrow} \{ \ddot{q} = -q - \zeta \dot{q} ; \dot{\zeta} = \dot{q}^2 - 1 \} .$$

Notice that the “momentum” p_s becomes the time-reversible friction coefficient ζ here.

Finally it can be confirmed that the three-dimensional Gaussian distribution function, in either (q, p, ζ) or (q, \dot{q}, ζ) space, is stationary so that the equations of motion are consistent with, and preserve, Gibbs’ canonical distribution:

$$f(q, \dot{q}, \zeta) \propto \exp[-(q^2 + \dot{q}^2 + \zeta^2)/2] \longrightarrow (\partial f/\partial t) = 0 .$$

It is noteworthy that the three-dimensional motion, unlike that in the four-dimensional (q, p, s, p_s) space, is compressible, $(\dot{\otimes}/\otimes) = -\zeta$, a change that becomes particularly interesting and important away from equilibrium. In the end the thermostatted motion equations and the canonical distribution have both emerged from Hamiltonian mechanics without the need for any time scaling or for considering the use of unequal timesteps in simulations. With Dettmann’s discovery these complexities of Nosé’s ideas are seen to be entirely unnecessary. In fact it is even simpler, and doesn’t require Hamiltonian mechanics at all, to use the phase-space continuity equation to derive a compressible version of Liouville’s Theorem, from which the Nosé-Hoover algorithm emerges in a natural way. This is next.

C. Hoover’s Route to Nosé-Hoover Dynamics in 1984

After lengthy stimulating conversations with Nosé in Paris, a few days prior to a meeting in Orsay, Bill sought to add a friction coefficient ζ to the Newtonian equations of motion while constraining the stationary probability density to Gibbs’ canonical-ensemble form:

$$\{ f(q, p, \zeta) \propto e^{-(q^2+p^2)/2} e^{-g(\zeta)} ; \dot{p} = -q - \zeta p \} \longleftrightarrow (\partial f/\partial t) \equiv 0 .$$

The continuity equation came in handy here. For a stationary probability density in the three-dimensional (q, p, ζ) space the sum of all six contributions to $(\partial f/\partial t)$ must vanish:

$$-f [(\partial \dot{q}/\partial q) + (\partial \dot{p}/\partial p) + (\partial \dot{\zeta}/\partial \zeta)] - \dot{q}(\partial f/\partial q) - \dot{p}(\partial f/\partial p) - \dot{\zeta}(\partial f/\partial \zeta) \equiv 0 .$$

The product form of the distribution function, with g depending only on ζ , turns out to satisfy the continuity equation in (q, p, ζ) space, with the control variable ζ regulating the

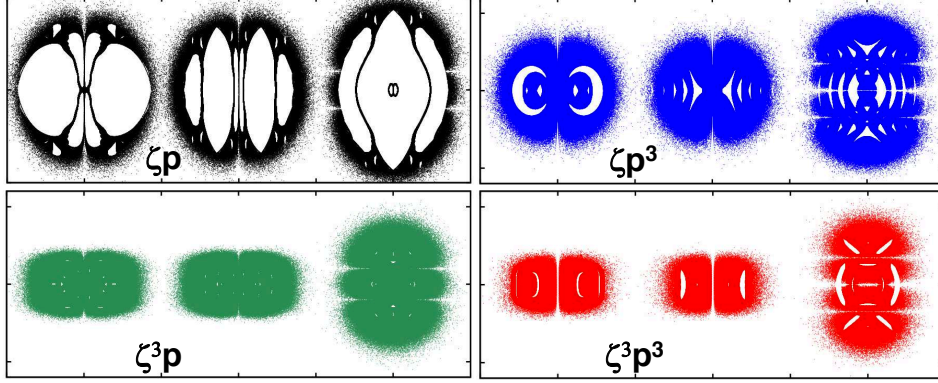


FIG. 8: $\{ \dot{q} = p ; \dot{p} = -q - \zeta^m p^n \}$ where $\dot{\zeta} = p^2 - 1$ for $n = 1$ and $\dot{\zeta} = p^4 - 3p^2$ for $n = 3$. The four simulations each used two billion timesteps with $dt = 0.003$. From left to right the Poincaré sections plot (p, ζ) , (q, ζ) , and (q, p) . The tic-mark spacing is five in each of these plots.

kinetic temperature by integral feedback, $\zeta \propto \int^t [p(t')^2 - 1] dt'$,

$$0 + f\zeta + 0 + fpq + f(-q - \zeta p)p + f\dot{\zeta}(dg/d\zeta) \equiv 0 \longrightarrow$$

$$g(\zeta) = (\zeta^2/2) ; \dot{\zeta} = p^2 - 1 .$$

This Nosé-Hoover approach is not at all unique. Bauer, Bulgac, and Kusnezov discuss the generality of such thermostating approaches and note particularly the usefulness of cubic forces in promoting “ergodicity”, the desirable property of accessing the entire distribution from any initial condition^{8,46}. In the case of the oscillator Nosé-Hoover dynamics is not at all ergodic. **figure 8** shows an improved approach toward ergodicity when cubic terms are included.

This prototypical harmonic oscillator example⁵⁵ only hints at the many applications of Nosé-Hoover dynamics. Though Nosé’s goal was the dynamical simulation of thermal equilibrium it is evident that such thermal boundary conditions can also be used to drive and analyze nonequilibrium steady states, the longstanding and elusive goals of researchers in statistical mechanics^{6,12–14,23}. Nosé’s incorporation of macroscopic temperature into the microscopic motion equations can be generalized to other types of applications in several ways: [1] to manybody systems at or away from equilibrium; [2] to ergodic distributions, by using more elaborate thermostats^{8,46}; and [3] to situations far from equilibrium⁵⁷.

In the manybody case it is feasible to apply different thermostat variables $\{ \zeta \}$ to different degrees of freedom and to control the local velocities as well as the kinetic temperature.

A straightforward route to ergodicity is to use two control variables rather than one^{28,48}, constraining both the second and the fourth moments of the velocity distribution:

$$\{ \dot{q} = p ; \dot{p} = -q - \zeta p - \xi p^3 ; \dot{\zeta} = (p^2 - 1) ; \dot{\xi} = (p^4 - 3p^2) \} \text{ [Hoover - Holian Oscillator] .}$$

In subsection III.h we will see detailed numerical evidence that these motion equations are indeed ergodic³⁵, filling out a four-dimensional Gaussian probability density,

$$f(q, p, \zeta, \xi) \propto e^{-[q^2 + p^2 + \zeta^2 + \xi^2]/2} .$$

Although these thermostatted algorithms have “frictional” control forces in addition to the usual forces derived from a potential function it is relatively easy to formulate time-reversible centered-difference algorithms to generate accurate trajectories. We explored this extension with Brad Holian and Tony De Groot and describe such an algorithm next for the Nosé-Hoover oscillator.

D. Centered Time-Reversible Algorithm for the Nosé-Hoover Oscillator

“Thermostatted” molecular dynamics such as the Nosé-Hoover or Hoover-Holian approach provides simulations at constant temperature. Let us demonstrate the feasibility of extending an algorithm of the Størmer-Verlet type to solve the Nosé-Hoover oscillator problem¹⁷. The harmonic oscillator, with the initial conditions $(q, p, \zeta) = (2.21, 0, 0)$ is an excellent example. The underlying differential equations can then be written in either one of two ways :

$$\begin{aligned} & \{ \dot{q} = p ; \dot{p} = -q - \zeta p ; \dot{\zeta} = p^2 - 1 \} \text{ or, equivalently} \\ & \{ \ddot{q} = -q - \zeta \dot{q} ; \dot{\zeta} = \dot{q}^2 - 1 \} \text{ [Nosé - Hoover Oscillator] .} \end{aligned}$$

The second-derivative form suggests a centered-difference analog:

$$q_{+dt} = 2q_0 - q_{-dt} + a_0 dt^2 - \zeta_0 (q_{+dt} - q_{-dt}) dt / 2 ; \zeta_{+dt} = \zeta_0 + dt [(q_{+dt} - q_0)^2 / dt^2 - 1] .$$

A convenient initial condition chooses the coordinate q at a turning point and the friction coefficient zero so that $q_{+dt} = q_{-dt} = q_0 + a_0 dt^2 / 2$. **figure 9** shows an accurate Runge-Kutta solution of the Nosé-Hoover oscillator with initial conditions $(q, p, \zeta) = (2.21, 0, 0)$ as a wide line with the centered-difference solution superimposed as a narrower line.

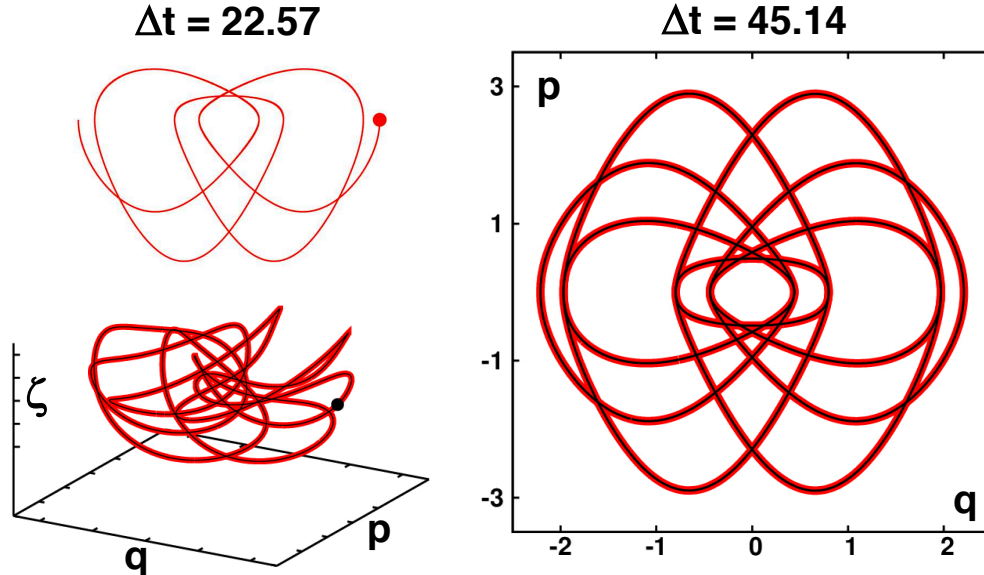


FIG. 9: Periodic trajectory of a thermostatted oscillator with $\{ \dot{q} = p ; \dot{p} = -q - \zeta p ; \dot{\zeta} = p^2 - 1 \}$. The initial conditions $(q, p, \zeta) = (2.21, 0, 0)$ are indicated by the red and black dots at the left. The first half of this periodic Nosé-Hoover orbit (upper left) is projected onto the $p(q)$ plane and shows nine trajectory crossings of the three-dimensional orbit (lower left) with $-2.5 < \zeta < +2.5$. The complete orbit shows 36 crossings. Fourth-order Runge Kutta and centered finite-difference integrator solutions are shown at the right after one billion timesteps $dt = 0.01$. The centered-difference algorithm remains close to this orbit for one billion timesteps with $dt = 0.1$ while fourth-order Runge-Kutta loses this orbit in favor of a knotless loop between $dt = 0.07$ and $dt = 0.08$ in billion-step simulations.

The centered-difference algorithm has a trio of advantages: stability, simplicity, and reversibility. The Runge-Kutta algorithm, detailed in the next subsection, is likewise straightforward and simple, though it lacks longtime stability and time-reversibility. Beyond these two useful approaches dozens of higher-order algorithms have been derived and implemented^{34,37}. All of them require more storage and more effort to reproduce. We illustrate the most useful of them here by applying it to a stiff, and therefore challenging example, the Nosé oscillator³⁷, illustrated in **figure 10**. The corresponding nonstiff Nosé-Hoover oscillator problem is shown there as well. A periodic Nosé-Hoover orbit appears in **figure 9**.

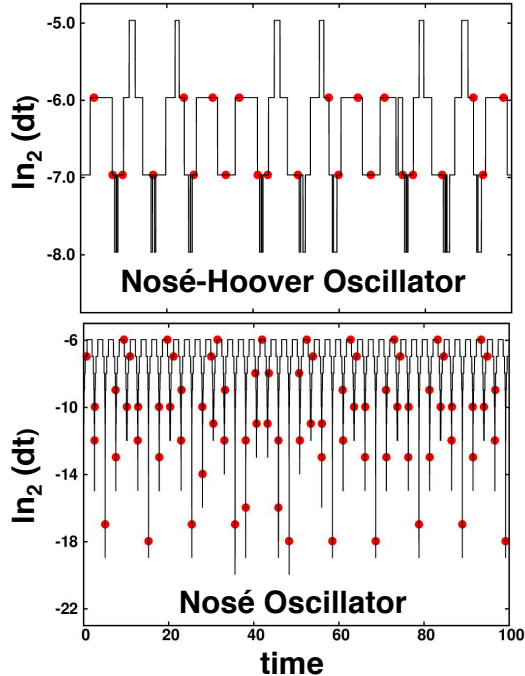


FIG. 10: The fourth-order adaptive Runge-Kutta integrator, with an rms error confined to the interval 10^{-12} to 10^{-10} shows that the stiffer Nosé equations require timesteps a thousand times smaller than do the Nosé-Hoover equations, though both trace out exactly the same $\{ q, p, s, \zeta \}$ trajectory (at quite different rates). The red dots indicate oscillator turning points where $p = 0$.

E. Fourth-Order Runge-Kutta Integrators

An advantage of Runge-Kutta integrators is that the timestep dt can be changed automatically in response to stiffness. By comparing the results of a single timestep to those of two half timesteps the rms discrepancy can be restricted to a prescribed interval by halving or doubling dt . A comparison of timestep histories for the stiff Nosé and nonstiff Nosé-Hoover oscillators is shown in **figure 10** with the details spelled out in reference 37.

Fourth-order Runge-Kutta integrations begin by selecting three additional points in the vicinity of the initial or current coordinate set of time-dependent variable, coordinates $q(t)$ and momenta $p(t)$ in the case of Hamiltonian mechanics:

$$q_1 = q(t) + \frac{dt}{2}\dot{q}(t) ; q_2 = q(t) + \frac{dt}{2}\dot{q}_1 ; q_3 = q(t) + dt\dot{q}_2 .$$

By expressing the derivatives at each of the four points as Taylor's series it is possible to choose coefficients giving an averaged derivative such that errors of order dt , dt^2 , dt^3 , and dt^4 all vanish, with the summed up coefficients equal to unity. Though this choice is not

unique the symmetric average, “classic Runge-Kutta”, is nearly always used:

$$q(t + dt) = q(t) + \frac{dt}{6} [\dot{q}(t) + 2\dot{q}_1 + 2\dot{q}_2 + \dot{q}_3] = q(t) + \frac{dt}{6} [p(t) + 2p_1 + 2p_2 + p_3] ,$$

giving an error of order $dt^5/5!$ and completing the algorithm. The algorithm requires a knowledge of the momentum $p = \dot{q}$ where p is advanced in just the same fashion as q , using the first-order set of motion equations $\{ \dot{q} = +p ; \dot{p} = -q \}$:

$$p(t + dt) = p(t) + \frac{dt}{6} [\dot{p}(t) + 2\dot{p}_1 + 2\dot{p}_2 + \dot{p}_3] = p(t) - \frac{dt}{6} [q(t) + 2q_1 + 2q_2 + q_3] .$$

Here too the Runge-Kutta algorithm has an analytic solution, but the oscillation is slightly damped, proportional to dt^6 . Although the algorithm is neither reversible nor conservative it is particularly simple to implement and is a first choice when thermostatted motion equations are introduced to carry out nonequilibrium simulations. The simplest such system is the Nosé-Hoover Oscillator. In the next subsection we apply the Runge-Kutta technique to a nonequilibrium version of the harmonic oscillator exposed to a specified temperature gradient (dT/dq), developed by Bill and Harald Posch in 1997 and revisited in 2014^{57,62}.

F. Nonequilibrium Nosé-Hoover Mechanics with $\mathbf{T}(\mathbf{q})$ and Knots

To begin, we generalize the Nosé-Hoover oscillator a bit by introducing the thermostat frequency parameter α and the temperature $T(q)$, which may be a nonconstant function of location for which we will choose $T(q) = 1 + \epsilon \tanh(q)$. Throughout we maintain the mass and force constant of the oscillator equal to unity.

$$\{ \dot{q} = p ; \dot{p} = -q - \zeta p ; \dot{\zeta} = \alpha(p^2 - T) \} [\text{Nosé - Hoover Oscillator}] .$$

When the temperature is constant we have seen that the Nosé-Hoover oscillator has a deceptively simple stationary state. The stationary probability density $f(q, p, \zeta)$ is a three-dimensional space-filling Gaussian :

$$\begin{aligned} f(q, p, \zeta) &\propto e^{-[q^2 + p^2 + (\zeta^2/\alpha)]/2} \xleftrightarrow{\text{NHQ}} \\ (\partial f / \partial t) &= -\partial(f\dot{q})/\partial q - \partial(f\dot{p})/\partial p - \partial(f\dot{\zeta})/\partial \zeta \xleftrightarrow{\text{NHQ}} \\ 0 &= -f [-\zeta - qp - p(-q - \zeta p) - (\zeta/\alpha)\alpha(p^2 - 1)] \equiv 0 . \end{aligned}$$

In 1985 Runge-Kutta solutions of the oscillator motion provided a stimulating surprise: at most, the numerical solutions for various thermostat strengths α occupied only small portions of this Gaussian²⁴.

For the Nosé-Hoover oscillator with $\alpha = 1$ the most common numerical solution type is a torus. There are infinitely many of these, with each of them centered on a stable one-dimensional periodic orbit in the three-dimensional (q, p, ζ) space. In addition to the tori, a definite fraction of the solutions explores a unique three-dimensional “chaotic sea”. Motion in that sea is “Lyapunov unstable”, meaning that small perturbations grow exponentially with time, an essential characteristic of chaos.

With $\alpha = 1$ and initial conditions for numerical solutions randomly drawn from the Gaussian stationary distribution, about six percent of the solutions trace out the three-dimensional chaotic sea⁵³. The remaining 94 percent give stable tori enclosing stable periodic orbits. The simultaneous existence of one-dimensional stable orbits with two-dimensional tori and unstable three-dimensional orbits, comprising the chaotic sea, all in close proximity to one another, was a surprise and heralded even more discoveries.

Soon after, in 2015, Wang and Yang showed that a stiffer higher-frequency thermostat, with $\dot{\zeta} = 10(p^2 - 1)$, provides *knots*, not just simple overhand or trefoil knots, but a wide and complex variety^{68,69}. In preparing this review we wondered whether or not such structures could also be found in the prototypical $\alpha = 1$ case. Investigation revealed a surprising complexity. We soon found the stable periodic orbit of **figure 9** with period 45.14 using $\alpha = 1$. The initial values (q, p, ζ) were $(2.21, 0, 0)$. In principle, such an orbit, embedded in three-dimensional space, can be analyzed according to a classical field of mathematics, “knot theory”.

Three-dimensional knots are now conventionally classified according to the number of crossings found in their two-dimensional projections⁴¹. Wikipedia states that there are over a million topologically distinct knots with 16 crossings, so that the knot shown in **figure 9**, with its 36 crossings, is likely well beyond the patience of even the most earnest of investigators. But this knot has a simplifying two-fold symmetry shown at the left. The initial half-period, $0 < t < 22.57$, is a mirror image of the second, $22.57 < t < 45.14$.

The two simpler half-period knots show only nine crossings. And manipulation of a plastic-chain model of them soon results in a topologically equivalent half-knot with just eight crossings, well within the range of analytic work as there are only 21 topologically

different eight-crossings knots. Because knot theory is an absorbing, challenging, and well-developed branch of mathematics, we expect it to contribute to the statistical mechanics of nonequilibrium systems through the study of models like the thermostatted oscillator considered here.

Let us now take leave of these singular periodic orbits to consider the fascinating world of ergodic Lyapunov-unstable oscillator dynamics. Ergodicity implies exploring the entire stationary distribution, for almost all initial conditions. Such dynamics can and do in fact achieve Nosé’s original goal of reproducing the entire canonical ensemble. The simplest of such dynamics was discovered by Clint Sprott in 2018⁶³. Its less-simple precursors date back to the 1990s.

G. Double Cross Sections / Numerical Methods

An even simpler route to simulating stationary nonequilibrium systems is to make the imposed temperature a function of coordinate. This can be accomplished with just the single degree of freedom describing a one-dimensional oscillator. To illustrate this idea consider a smooth temperature profile reminiscent of a shockwave:

$$T(q) = 1 + \epsilon \tanh(q).$$

The oscillator friction coefficient ζ can then react to the local temperature $T(q)$:

$$\{ \dot{q} = p ; \dot{p} = -q - \zeta p ; \dot{\zeta} = p^2 - T(q) \} .$$

In the following subsection we will consider a surprise which results from this simple nonequilibrium problem, an astonishing complexity of oscillator orbits in the form of topological *knots*, an active mathematical field, with 1898 arXiv papers now listed under “knot theory”.

Two of these occurred in 1997⁵⁷ and 2014⁶². With Harald Posch, in 1997, Bill found that exposing a harmonic oscillator to a coordinate-dependent temperature, $T(q) = 1 + \epsilon \tanh(q)$, can result in another qualitatively different solution type, fractal (fractional-dimensional) phase-space distributions. Such fractals are “dissipative”, with time-averaged vanishing phase-space volume in response to overall positive “friction” from the control variable ζ :

$$\langle \dot{\otimes}/\otimes \rangle = \langle -\zeta \rangle < 0 \longleftrightarrow \langle p^3/2 \rangle \propto -\nabla T < 0 \text{ [Fractal Solutions]} .$$

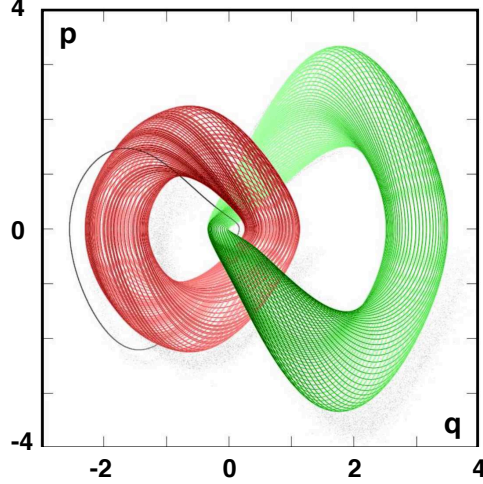


FIG. 11: $\{ \dot{q} = p ; \dot{p} = -q - \zeta p ; \dot{\zeta} = p^2 - [1 + 0.42 \tanh(q)] \}$ with initial conditions $(-2.7, 0, 0)$ [limit cycle], $(-2.3, 0, 0)$, and $(+3.5, 0, 0)$ [tori] showing the interlocked nature of the three distinct solutions of exactly the same nonequilibrium Nosé-Hoover motion equations.

These chaotic trajectories invariably converge to stationary nonequilibrium flows of kinetic energy $p \times (p^2/2)$ in the hot-to-cold direction. Though Lyapunov unstable, with chaos, the flows are stable from the thermodynamic viewpoint, satisfying the Second Law.

With Clint Sprott, in 2014, we discovered that a pair of dissimilar two-dimensional conservative tori can coexist, while simultaneously interlocked with a nonequilibrium dissipative limit cycle. On the one hand, like the phase-space fractals, the limit cycle supports dissipation, phase-volume loss, and net hot-to-cold heat flow. On the other hand, the mutually interlocked conservative tori have no net heat flow, $\langle p \times (p^2/2) \rangle$ – nor do they show any tendency for phase-volume loss:

$$\langle -\dot{\otimes}/\otimes \rangle = -\langle (\partial\dot{p}/\partial p) \rangle = +\langle \zeta \rangle \equiv 0 \text{ [Conservative Tori]} .$$

figure 11 shows this situation where the oscillator dynamics of the friction coefficient ζ is constrained by a moderate imposed local temperature, with $\epsilon = 0.42$:

$$T(q) = 1 + \epsilon \tanh(q) \rightarrow \nabla T = \epsilon / \cosh^2(q) :$$

$$\{ \dot{q} = p ; \dot{p} = -q - \zeta p ; \dot{\zeta} = p^2 - T(q) \} \text{ [Nonequilibrium Oscillator]} .$$

Runge-Kutta integration of these motion equations with $\epsilon = 0.42$ gives numerical estimates for the time-averaged loss of phase volume and the heat flux:

$$\langle \dot{\otimes}/\otimes \rangle = \langle (\partial\dot{p}/\partial p) \rangle = \langle -\zeta \rangle = -0.105 ; \langle p^3/2 \rangle = -0.259 .$$

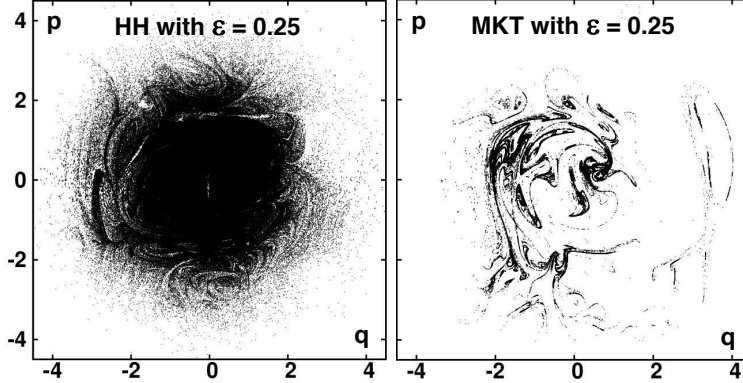


FIG. 12: Double $p(q)$ conducting oscillator cross sections with $\zeta^2 + \xi^2 < 0.00001$. The greatly enhanced equilibration of the stiffer Hoover-Holian thermostat relative to the gentler Martyna-Klein-Tuckerman thermostat is apparent.

Notice again that each of the three solutions pictured is interlocked with the other two.

Graphical explorations in three or four dimensions can be based on sections of or projections onto two-dimensional surfaces. In the absence of dissipation the Hoover-Holian and Martyna-Klein-Tuckerman oscillators equations have the same stationary solution, Gaussian in all four variables (q, p, ζ, ξ) . The presence of an imposed temperature gradient can cause the Gaussians to condense onto fractal attractors of reduced information dimension.

Let us illustrate with a moderate temperature gradient, $T(q) = 1 + 0.25 \tanh(q)$. We incorporate this feature into the equations of motion as follows:

$$\{ \dot{q} = p ; \dot{p} = -q - \zeta p - \xi p^3 ; \dot{\zeta} = p^2 - T(q) ; \dot{\xi} = p^4 - 3p^2 \} [\text{HH}] ;$$

$$\{ \dot{q} = p ; \dot{p} = -q - \zeta p ; \dot{\zeta} = p^2 - T(q) - \xi \zeta ; \dot{\xi} = \zeta^2 - T(q) \} [\text{MKT}] .$$

The structure of the resulting fractals can then be explored through double cross sections in which two of the four time-dependent variables take on specified values as is illustrated in **figure 12**.

H. MKT, HH, 0532, and Sprott Routes to Ergodicity

Because Nosé's goal, a deterministic dynamics reproducing Gibbs' canonical distribution, was eluded by the prototypical oscillator problem it was natural to modify Nosé-Hoover mechanics in an attempt to achieve ergodicity. Two successful approaches^{28,48} added a

second control variable to ζ :

$$\{ \dot{q} = p ; \dot{p} = -q - \zeta p ; \dot{\zeta} = p^2 - 1 - \xi \zeta ; \dot{\xi} = \zeta^2 - 1 \text{ [MKT] } ;$$

$$\{ \dot{q} = p ; \dot{p} = -q - \zeta p - \xi p^3 ; \dot{\zeta} = p^2 - 1 ; \dot{\xi} = p^4 - 3p^2 \text{ [HH] } .$$

Both approaches trace out exactly the same stationary state, a Gaussian in all four variables. The Martyna-Klein-Tuckerman approach can be generalized to add “chains” of thermostat variables. The Hoover-Holian approach can also be generalized further, but only a little, and at the expense of excessive stiffness, by adding control of the sixth moment, $\langle p^6 \rangle$.

It is interesting to note that the fluctuations in the rate at which phase space is explored, despite the identical distributions, are much larger in the HH case. The mean-squared value $\langle \dot{\zeta}^2 \rangle$ is $\langle p^8 - 6p^6 + 9p^4 \rangle = 105 - 90 + 27 = 42$ for the HH equations and only $3 - 2 + 1 = 2$ in the MKT case. The relative stiffness of the Hoover-Holian equations is the underlying reason why the sixth-moment analog of the HH equations was long thought to be unstable.

The search for ergodic thermostats based on a single control variable rather than two, eventually bore fruit. Brute-force exploration of parameter space revealed that the “0532” oscillator, with “weak control” of both the second and fourth moments, is in fact ergodic:

$$\{ \dot{q} = p ; \dot{p} = -q - \zeta [0.05p + 0.32p^3] ; \dot{\zeta} = 0.05(p^2 - 1) + 0.32(p^4 - 3p^2) \} \text{ [0532] } .$$

In 2017 another single-control approach was the result of Tapias-Bravetti-Sanders’ prize-winning variant of the Nosé-Hoover oscillator⁶⁵ :

$$\{ \dot{q} = p ; \dot{p} = -q - 10 \tanh(5\zeta)p ; \dot{\zeta} = p^2 - 1 \} \text{ [TBS] } .$$

The next year Sprott, noting that a limiting case of TBS control is “bang-bang” (or “on-off”) control, suggested switching the friction coefficient discontinuously, $\pm\alpha \longleftrightarrow \mp\alpha$, based on the kinetic temperature’s history⁶³. Sprott termed this singular model a “Signum Thermostat” as it depends only on the sign and not the magnitude of the friction coefficient ζ :

$$\{ \dot{q} = p ; \dot{p} = -q - \alpha (\zeta / |\zeta|) p ; \dot{\zeta} = p^2 - 1 \} , \text{ [Sprott’s Signum Oscillator] } .$$

Sprott found that a sufficiently large value of $\alpha > 1.7$ provides an ergodic oscillator. This problem is instructive in that programming a precise interpolation to find the times at which ζ vanishes just adds to the difficulty of carrying out an adaptive integration. It is simpler

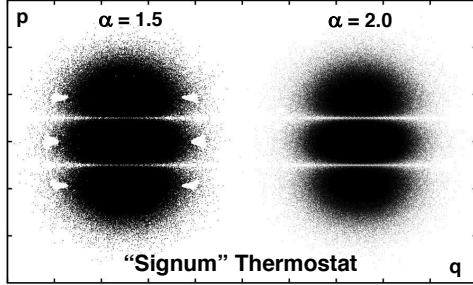


FIG. 13: $\{ \dot{q} = p ; \dot{p} = -q - \alpha(\zeta/|\zeta|)p ; \dot{\zeta} = p^2 - 1 \}$. A hyperbolic tangent approximation to Sprott’s “Signum” thermostat applied to the harmonic oscillator: $(\zeta/|\zeta|) \rightarrow \tanh(400\zeta)$. These (q, p) Poincaré sections with $\zeta = 0$ were generated with one billion timesteps, $dt = 0.001$. The six holes to the left correspond to stable periodic tori. With $\alpha = 2$ the motion is ergodic.

and straightforward to solve the motion equation $\dot{p} = -q - \alpha \tanh(400\zeta)p$ rather than the singular signum limit. We have adopted this simplification in **figure 13**.

In none of these cases is ergodicity proven. But several convincing numerical tests can be applied. In 2015 we applied six of them to the MKT oscillator³⁵. TBS provided more. Three of these tests are relatively simple: [1] A Gaussian distribution with unit standard deviation should reproduce its nonzero even moments, $\{ 1, 3, 15, 105, \dots \}$; [2] A Poincaré section cutting through the distribution must reveal no holes; and [3] The largest Lyapunov exponent λ_1 must have the same long-time-averaged positive value independent of the initial condition. All of these computational tests are relatively simple to administer.

A relatively stringent test of the four-dimensional Gaussians’ “no holes” criterion can be based on the construction of a “double cross section”, plotting values of two of the four variables whenever the remaining two are sufficiently close to zero. Points for the (q, p) section of the MKT oscillator can be collected whenever $(\zeta^2 + \xi^2) < 0.00001$, for instance. A convincing Gaussian results. On the other hand points for the (ζ, ξ) section with $(q^2 + p^2) < 0.00001$ look rather peculiar⁵². This is because there is no motion perpendicular to the (q, p) plane where both variables vanish, so that

$$\{ \dot{q} = 0 ; \dot{p} = 0 ; \dot{\zeta} = -1 - \zeta\xi ; \dot{\xi} = \zeta^2 - 1 \} .$$

These (ζ, ξ) equations are isomorphic to those of a falling particle, with speed ζ , controlled by a friction coefficient ξ maintaining a “kinetic temperature” $\langle \zeta^2 \rangle$ of unity. Let us describe that closely-related problem next.

I. Nosé-Hoover Mechanics for the Falling Particle

Our book written in Japan in 1989-1990, *Computational Statistical Mechanics*²⁵, contains an interesting example of Nosé-Hoover mechanics in which coordinates make no explicit appearance. Coordinates can instead be introduced implicitly by integrating the momentum, $p = \dot{q}$. Their absence is reminiscent of the disappearance of Nosé’s time-scaling variable s , which can be calculated from the Nosé-Hoover equations by integrating the friction coefficient, $\zeta = (\dot{s}/s)$. Now to the Nosé-Hoover example.

We consider a thermostatted particle with momentum p under the influence of a constant external gravitational field and a time-reversible frictional force $-\zeta p$. Just as in the oscillator problems we simplify this example by choosing the mass, gravitational field strength, thermostat frequency, temperature, and the geometric dimensionality of the problem all equal to unity. The prototypical equations of motion for the falling particle become

$$\{ \dot{p} = -1 - \zeta p ; \dot{\zeta} = p^2 - 1 \} \text{ [Falling Particle] .}$$

Compare these to the motion equations in the $\{ q = 0, p = 0 \}$ plane for the MKT oscillator:

$$\{ \dot{\zeta} = -1 - \xi \zeta ; \dot{\xi} = \zeta^2 - 1 \} \text{ [MKT Oscillator in the } (0, 0, \zeta, \xi) \text{ plane] .}$$

The two problems, a falling particle and an ergodic oscillator’s $(0, 0, \zeta, \xi)$ plane motion are one and the same! All these equations are time-reversible, in that any solution with positive dt can be used to find a solution with negative dt by changing the signs of p , ζ , and ξ .

Both sets of motion equations have two fixed points, the unstable repellor “source”, at (p, ζ) or $(\zeta, \xi) = (+1, -1)$ and the stable attractor “sink” at (p, ζ) or $(\zeta, \xi) = (-1, +1)$. The repellor and attractor for the dissipative falling-particle flow are just “fixed points” in this simplest example problem rather than the complex fractal objects familiar from more complicated flows. The flow equations describe a time-reversible dissipative repellor-to-attractor flow from $(+1, -1)$ to $(-1, +1)$. See **figure 14**. Changing the signs of both dependent variables as well as the time generates trajectories approaching the attractor (purple) and the repellor (green).

A linear stability analysis of the flow in the neighborhood of the fixed points provides a detailed understanding of the problem. We begin at the attractor $(-1, +1)$ and describe the offset from that fixed point by introducing two infinitesimal offset variables, (δ_p, δ_ζ) :

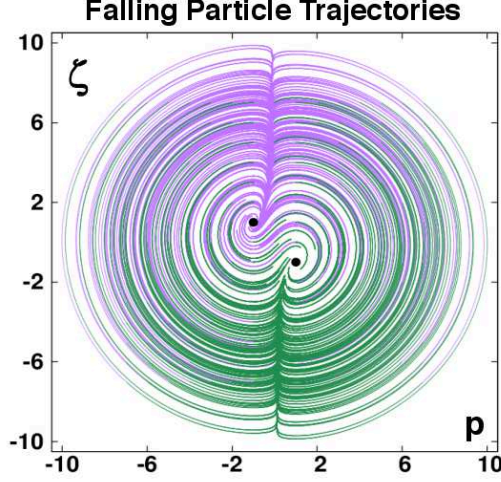


FIG. 14: Time histories of 225 points initially located on a square grid from -7 to $+7$ in p and ζ , followed for a time of $\pm 3 = 3000dt$ forward (purple) and backward (green) toward the attractor at $(-1, +1)$ and the repeller at $(+1, -1)$, both indicated by black dots.

$\delta_p \equiv p + 1$ and $\delta_\zeta \equiv \zeta - 1$. From the Falling Particle equations above we then find the equations of motion for δ_p and δ_ζ :

$$\begin{aligned} \dot{\delta}_p &\simeq -\zeta\delta_p - p\delta_\zeta \simeq -\delta_p + \delta_\zeta \longrightarrow \ddot{\delta}_p = -\dot{\delta}_p - 2\delta_p ; \\ \dot{\delta}_\zeta &= 2p\delta_p \simeq -2\delta_p \longrightarrow \ddot{\delta}_\zeta \simeq -2\dot{\delta}_p \simeq 2\delta_p - 2\delta_\zeta = -\dot{\delta}_\zeta - 2\delta_\zeta . \end{aligned}$$

The two linear second-order equations for δ_p and δ_ζ have solutions proportional to $e^{i\omega t}$ where substitution of that form of the solution gives the result :

$$\omega^2 - i\omega - 2 = 0 \longrightarrow \omega = (i/2) \pm \sqrt{7/4} .$$

figure 15 displays the logarithms of the *squared* offset components (so as to have real logarithms) for both the repeller and the attractor. Because for small offsets the dependence is proportional to $e^{\pm t/2}$ the logarithms of the squares have a slope of unity when plotted as functions of time. Counting the oscillations confirms the accuracy of the linear analysis just given.

The falling-particle flow itself has an interesting and stimulating stationary global solution for the probability density $f(p, \zeta, t)$ which can be written in either of two forms. Here are both:

$$f(p, \zeta, t) \propto e^{-(p^2/2) - (\zeta^2/2) - \int_0^t p(t') dt'} \equiv e^{+ \int_0^t \zeta(t') dt'} .$$

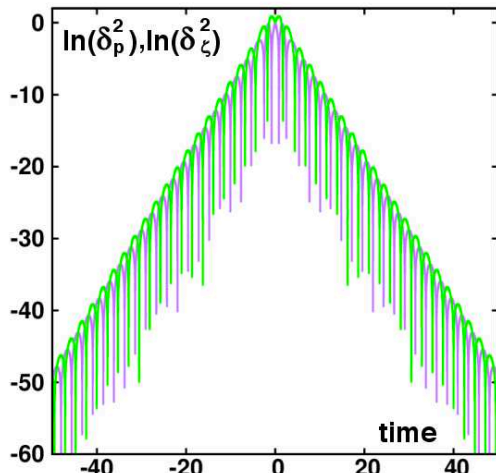


FIG. 15: Logarithms of the squared offsets δ_p^2 and δ_ζ^2 from the repellor and attractor starting at $(0,0)$ and going both forward to the attractor and backward toward the repellor for a time of 50. The slope of unity and the oscillation frequency from the 21 maxima corresponding to 10.5 periods agree perfectly with the linear stability analysis given in the text.

We can confirm the two expressions simultaneously by showing that there is a constant of the motion, C for the flow:

$$C \equiv (p^2/2) + (\zeta^2/2) + \int_0^t p(t')dt' + \int_0^t \zeta(t')dt' \longrightarrow$$

$$\dot{C} = p\dot{p} + \zeta\dot{\zeta} + p + \zeta = p(-1 - \zeta p) + \zeta(p^2 - 1) + p + \zeta \equiv 0 .$$

figure 15 describes a particular solution of these model equations centered on $(0,0)$ and proceeding either forward or backward by choosing the appropriate sign for the timestep dt .

By introducing more complexity in the falling-particle model, with a more elaborate thermostat (HH or MKT) and with two space dimensions rather than just one, a variety of interesting nonequilibrium states can be constructed and analyzed. This appears to be an excellent problem for elaboration and exploration. We recommend it for further study.

IV. LYAPUNOV EXPONENTS, HEAT FLOW, FRACTALS, AND SHOCKWAVES

Linear differential equations have exponential solutions, real, imaginary, or complex, as typified by biological growth, mechanical dissipation, or periodic oscillations. Driven, damped, and underdamped oscillators provide the simplest examples of these three possibilities. Manybody classical systems are typically “Lyapunov unstable”. This means that a

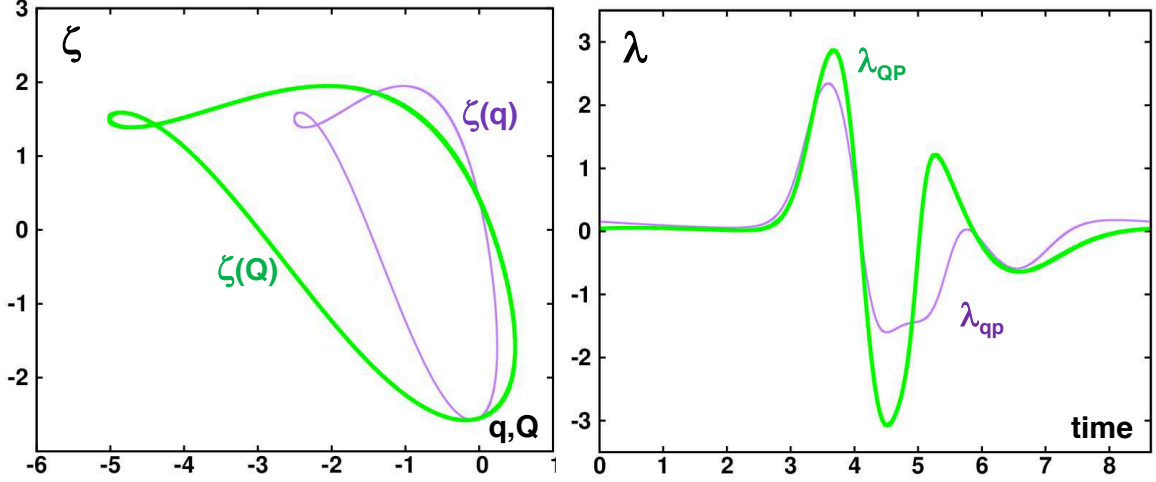


FIG. 16: This figure demonstrates that the local Lyapunov exponent $\lambda_1(t)$ depends on the coordinate system choice for the Nosé-Hoover oscillator, corresponding to choosing $s = 1$ or 2 .

small change is amplified exponentially fast by the dynamics. In an N -dimensional phase-space representation of the dynamics we can imagine defining a spectrum of growth rates $\lambda_1 \dots \lambda_N$ by measuring the expansion or contraction of a comoving hypersphere or hypercube. Practical measurement algorithms for these exponents were developed by Shimada and Nagashima⁶¹ and Benettin’s group⁷ forty years ago, and are relatively easy to implement, requiring only continuous attention to maintain the orthogonality of the vectors representing the directions in which the dynamical expansions and contractions occur. Let us consider here a familiar three-dimensional example, the thermostatted Nosé-Hoover oscillator. This problem has an unfamiliar moral.

In Hamiltonian mechanics the conservation of phase volume, derived through Liouville’s Theorem, $(\dot{\otimes}/\otimes) = \sum \lambda_i \equiv 0$, guarantees that the sum of all the Lyapunov exponents vanishes for Hamiltonian systems. Time-reversibility correctly suggests that these exponents come in pairs, $\{ \pm\lambda \}$, with the signs expressing expansion or contraction corresponding to following the motion either forward or backward in time. Although the time-reversibility of thermostatted nonequilibrium systems certainly suggests this same pairing of positive and negative exponents, in practice the possibility of dissipation, forming a chaotic “strange attractor” in the state space, is seized upon by the dynamics. The Nosé-Hoover oscillator in a temperature gradient provides a simple example problem where the “time-reversible” “attractor” actually gives way to an irreversible one-dimensional limit cycle³³. In **figure 16**

two different coordinate systems describe the same periodic orbit:

$$\{ \dot{q} = p ; \dot{p} = -q - \zeta p ; \dot{\zeta} = p^2 - T(q) \} ; T = 1 + 0.5 \tanh(q) \text{ with } s = 1 ;$$

$$\{ \dot{Q} = 4P ; \dot{P} = -(Q/4) - \zeta P ; \dot{\zeta} = 4P^2 - T(Q) \} ; T = 1 + 0.5 \tanh(Q/2) \text{ for } s = 2 .$$

The relationship between the two coordinate systems illustrated here is the simplest possible: $(q, p) \rightarrow (Q/s, sP)$. Here both $s = 1$ (purple) and $s = 2$ (green) are illustrated. The two limit cycles, both with period 8.65, were obtained after discarding ten million timesteps $dt = 0.001$ from the initial conditions $(q, p, \zeta) = (0, 5, 0)$. The subsequent time dependence of the friction coefficient $\zeta(t)$ (at the left) is independent of s but the local values of the time-dependent exponents depend upon the scale factor s , with the largest local Lyapunov exponent illustrating this dependence at the right.

Despite the time-reversibility of these motion equations symmetry breaking promptly finds the limit-cycle solution illustrated in **figure 16**. Investigation reveals that the largest of the three Lyapunov exponents has time-averaged value zero, and can be thought of as reflecting the time-averaged lack of expansion or contraction of a vector parallel to the periodic dynamical (q, p, ζ) trajectory.

A thorough dynamical description of the motion is more complicated than the single-exponent example of **figure 16**. Computing all three Lyapunov exponents requires the solution of 12 ordinary differential equations. Three of the motion equations describe an underlying reference trajectory. The additional nine characterize the directions of three co-moving and corotating orthogonal offset vectors. The offsets are “small” displacements from the reference trajectory. The vectors, typically of length 10^{-5} when the reference trajectory variables are of order unity, can be described in the same three-dimensional (q, p, ζ) state space as the reference trajectory. Alternatively the equations of motion can be linearized around the values of the nearby reference trajectory:

$$\{ \dot{\delta}_q = \delta_p ; \dot{\delta}_p = -\delta_q - \zeta \delta_p - p \delta_\zeta ; \dot{\delta}_\zeta = 2p \delta_p - (dT/dq) \delta_q \} ,$$

with infinitesimal offset vectors taken to be of unit length⁵⁸.

In either case constraints maintaining the lengths and orthogonality of the three vectors can be imposed on the motion by six Lagrange multipliers²⁷, three maintaining orthogonality and three maintaining the vector lengths, with the latter giving the three local Lyapunov exponents, $\{ \lambda_i(t) \}$. When time-averaged these exponents, $\{ 0, -0.0715, -0.2225 \}$, sum

to give the time-rate-of-change of the comoving three-dimensional volume, showing that an infinitesimal cylinder moving with the trajectory shrinks radially toward the limit cycle ;

$$\langle \langle \dot{\otimes}/\otimes \rangle \rangle = \langle \langle \partial\dot{q}/\partial q \rangle + \langle \partial\dot{p}/\partial p \rangle + \langle \partial\dot{\zeta}/\partial \zeta \rangle \rangle = \langle \langle 0 - \zeta + 0 \rangle \rangle = \lambda_1 + \lambda_2 + \lambda_3 = -0.2940 .$$

The straightforward ‘‘Gram-Schmidt’’ algorithm maintains the orthogonality and orthonormality of the offset vectors and can be applied at every timestep. The first offset vector, which determines the exponent $\lambda_1(t)$, is simply rescaled in length at every timestep so as to determine the local exponent:

$$\lambda_1 \equiv (1/dt) \ln[(\delta_{\text{before}}/\delta_{\text{after}})] .$$

The second offset vector then undergoes two constraints: [1] orthogonality with δ_1 is first imposed, by subtracting that fraction of δ_2 which parallels δ_1 . [2] the length of δ_2 is then rescaled, giving the second local Lyapunov exponent $\lambda_2(t)$: $\lambda_2 \equiv (1/dt) \ln[(\delta_{\text{before}}/\delta_{\text{after}})]$. The alternative Lagrange-multiplier constraints require only occasional applications of the Gram-Schmidt orthonormality algorithm to offset the inevitable effects of roundoff error. In manybody systems the Lyapunov spectra often exhibit a powerlaw form reminiscent of the Debye Model’s vibrational frequencies of a continuum⁵⁶. The time-averaged spectrum of Lyapunov exponents, unlike the local instantaneous spectra, has a very interesting connection to the Second Law of Thermodynamics. We describe it in the next subsection for a family of one- and two-dimensional manybody problems exhibiting heat conductivity and interesting Lyapunov spectra.

A. Fractal Dimensionality Loss for 24 ϕ^4 Particles³⁰

The thermostat forces generalizing Nosé’s work to nonequilibrium systems make it possible to study ‘‘mesoscopic’’ systems, small enough for an atomistic description but large enough to be described with continuum concepts. The simplest such system is the ϕ^4 model, a regular lattice, one-, two-, or three-dimensional, of particles tethered to lattice sites with a quartic potential and with additional nearest-neighbor Hooke’s-Law harmonic forces. In 2004 two-dimensional ϕ^4 models provided an excellent testbed for comparing a variety of thermostat forces. We carried out a thorough comparison of seven distinct thermostat types, all of them applied to two-dimensional models with four thermostatted cold

particles at a cold-end kinetic temperature of 0.5 and four thermostatted hot particles at a hot-end temperature of 1.5. 16, 32, or 64 Newtonian particles were sandwiched between the two thermostatted columns³¹. Series of simulations for the different system sizes and different thermostats suggested that the various approaches would agree for large systems. Deviations from this imagined large-system limit could be estimated for each of the thermostats. In the end this work reached a simple conclusion :

“The simplicity of thermostats based on the second moment of the velocity distribution and simply connected to irreversible thermodynamics recommends the use of Nosé-Hoover thermostats whenever possible.”

B. An Educational One-Dimensional Model of Heat Flow

The encouraging nature of the two-dimensional simulation results led us to subsequent investigations of somewhat longer one-dimensional ϕ^4 chains³⁶. **figure 17** describes the Lyapunov instability of a typical 24-atom chain. The figure shows the largest sixteen Lyapunov exponents from the spectrum of 50. The 50-dimensional phase space is composed of 24 coordinates, 24 momenta, and two Nosé-Hoover friction coefficients. The two thermostats maintain time-averaged kinetic temperatures of 0.003 and 0.027 at the two ends of the 24-particle chain. The tethering force constant, the Hooke’s-Law force constant, and the particle masses were all taken equal to unity. To illustrate, the motion equations of the first (cold) particle and its neighbor in the chain are as follows:

$$\dot{\zeta}_1 = \dot{q}_1^2 - 0.003 ; \ddot{q}_1 = -q_1^3 + (q_2 - q_1) - \zeta_1 \dot{q}_1 ; \ddot{q}_2 = -q_2^3 + (q_1 + q_3 - 2q_2) .$$

Here the particle coordinates $\{ q \}$ are measured relative to their fixed lattice positions. The Lyapunov exponents summed-up at the right in **figure 17** show that a 15-dimensional hypervolume in the phase space expands exponentially with time while a 16-dimensional hypervolume contracts. Evidently the fractal dimension of the strange attractor (between 15 and 16) lies below that of the phase space by a “dimensionality loss” of at least 34, about 70 percent of the total. This feature of time-reversible dynamical systems is striking in its significance and generality. With this specific microscopic case in mind let us consider a corresponding “thought experiment” close to macroscopic thermodynamics and its Second Law.

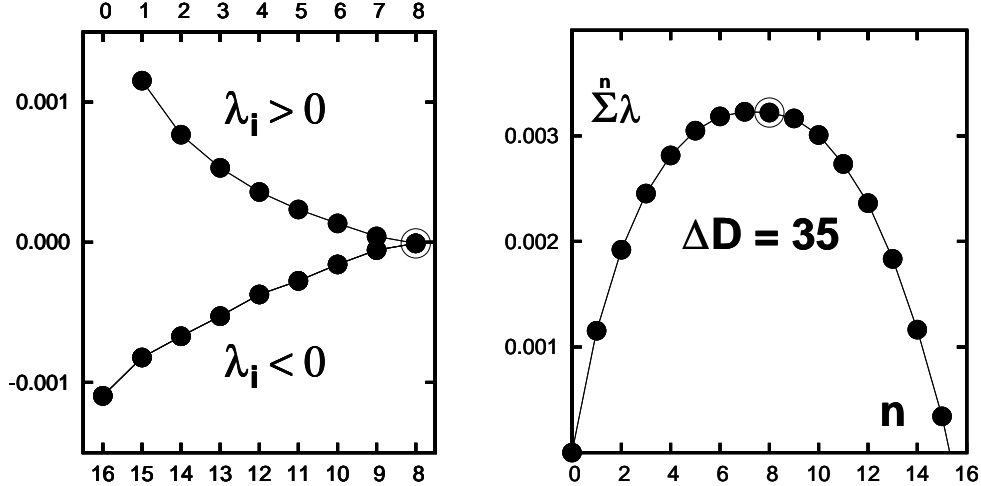


FIG. 17: A part of the 50-exponent Lyapunov spectrum of a conducting ϕ^4 chain is shown at the left where Nosé-Hoover thermostats maintain boundary temperatures (of a single cold and single hot particle) at 0.003 and 0.027. At the left we see seven positive exponents, a zero (corresponding to the lack of a time-averaged expansion or contraction along the trajectory direction in phase space), and eight negative exponents, just enough to furnish a negative overall sum, placing the dimensionality of the steady-state strange attractor between 15 and 16. At the right the sums of exponents are plotted. For more details see references 30 and 36.

C. Macroscopic Heat Flow and the Second Law of Thermodynamics

Imagine a conducting solid with many degrees of freedom connected to two time-reversible heat reservoirs with different temperatures, one “cold” and the other “hot”, just as in the 24-particle model example above. Imagine that this macroscopic solid body obeys Fourier’s Law, with a heat flux proportional to the local temperature gradient, $Q \propto -\nabla T$. We expect that on a time-averaged basis heat would flow from the hot reservoir through the system to the cold reservoir at a rate proportional to the temperature difference between the reservoirs. The consequent thermodynamic rate of increase in the solid’s entropy at the hot reservoir, $\simeq Q/T_{\text{hot}}$, is then more than offset by the larger rate of entropy decrease at the cold reservoir $\simeq Q/T_{\text{cold}}$. The greater loss at T_{cold} leads to the embarrassing conclusion that in a heat-conducting steady state the system entropy inexorably diverges to minus infinity! The conventional cure for this straightforward conclusion is to imagine an “entropy production” inside the system chosen exactly to offset the net entropy loss at the reservoir-system boundaries. Without this *ad hoc* assumption the entropy changes *at* the boundaries

would sum to zero rather than to the positive result required by the Second Law: the entropy of the “Universe” (system plus reservoirs here) approaches a maximum.

Evidently the macroscopic analysis of this thought experiment is not particularly informative. If we instead consider the alternative microscopic point of view, imagining that Nosé-Hoover heat reservoirs maintain the hot and cold boundary temperatures, we can develop time-averaged equations relating the energy extracted from the solid to the summed-up hot and cold friction coefficients and to the volume change in phase space:

$$\sum \langle \zeta p^2 / mkT \rangle \equiv \sum \langle \zeta \rangle = \sum \langle (-\partial p / \partial p) \rangle = \langle (-\dot{\otimes} / \otimes) \rangle = \langle -(\dot{S} / k) \rangle .$$

Here the time-averaged equality of ζp^2 and ζmkT follows from the vanishing of the averaged time derivative of a bounded quantity $0 = \langle \frac{d}{dt}(\zeta^2/2) = \zeta \dot{\zeta} \rangle \propto \langle \zeta(p^2 - mkT) \rangle$.

The formation of fractal attractors and repellers in the phase space is thoroughly consistent with macroscopic thermodynamics. Nonequilibrium microstates, both the repellor and the attractor, are both so rare as to have zero measure in the equilibrium phase space, due to dimensionality loss. The fractal attractor is stable, with shrinking phase volume, while the repellor is not, making its observation impossible. A simulation beginning with a reversed heat flow and reversed friction coefficients quickly illustrates its numerical instability by returning to its mirror-image attractor. The compatibility of the paired attractors and repellers in nonequilibrium systems became apparent in 1987^{16,26,49} and supports the use of reversible thermostats in modelling nonequilibrium systems. Simulations of shear and heat flow have a long history and a record of good agreement with experimental values⁶. Let us turn to systems which are not yet so well understood, systems in which the transport is nonlinear, shockwaves.

D. Macroscopic and Microscopic Shockwave Models

Nonequilibrium systems involve dissipation, irreversibility, and boundary conditions linking the system to the outside world, which drives it away from equilibrium. In modelling nonequilibrium stationary states the heat generated inside the system is extracted by external heat reservoirs. The simplest nonequilibrium steady states, shear flow and heat flow, require transport of momentum and energy *through* such a system. Such nonequilibrium steady states can be described by a variety of models, of which the macroscopic Navier-

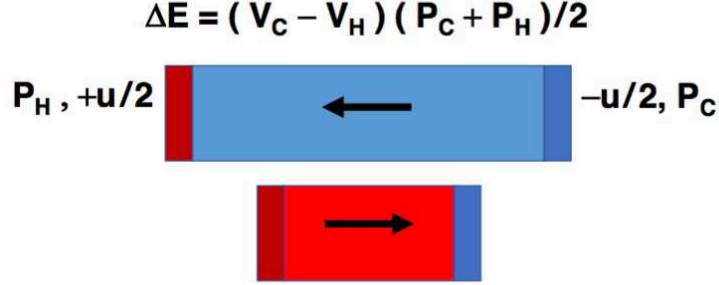


FIG. 18: Illustrating the shockwave conversion of work to heat as described by the Rankine-Hugoniot relation. Left-moving cold fluid is transformed to right-moving hot fluid (with exactly the same kinetic energy and with the additional “internal” energy $E_{\text{hot}} - E_{\text{cold}}$) through the fluid’s reaction to the work done on it by the two moving pistons: $\Delta E = P_{\text{cold}}\Delta V/2 + P_{\text{hot}}\Delta V/2$.

Stokes equations and the microscopic Boltzmann Equation are the simplest representatives. A host of simulations of the viscosities shear and bulk, and the heat conductivity have been carried out and found to give useful results despite the effects of boundaries.

Here we focus on phenomena for which the boundary conditions are purely equilibrium, as in the interface between coexisting phases, but with the boundary between different states characterized by different velocities. Let us consider a steady “one-dimensional” (meaning planar) shockwave, with cold low-pressure material transformed to a higher-pressure higher-temperature compressed state by motion of a steady wave. We begin by indicating a predictive path to the steady structure of such a wave.

E. Macroscopic Shockwaves from the Navier-Stokes Equations^{15,22}

The two simplest transport processes appear together in sound waves, which decay, and in shockwaves, where a steady input of fast-moving cold fluid is converted to a slower hotter output state by a localized nonequilibrium process. The macroscopic Rankine-Hugoniot Equations, dating back to the nineteenth century, are most easily derived by imagining the nonequilibrium conversion of a left-moving fluid to right-moving with equal speeds but opposite velocities before and after. As the kinetic energy is unchanged the internal energy increase is equal to the work done:

$$(P_{\text{hot}} + P_{\text{cold}})(1/2)(V_{\text{cold}} - V_{\text{hot}}) = (e_{\text{hot}} - e_{\text{cold}}) \text{ [Rankine - Hugoniot Equation]} .$$

Though the Rankine-Hugoniot equation expressed in **figure 18** correctly describes the

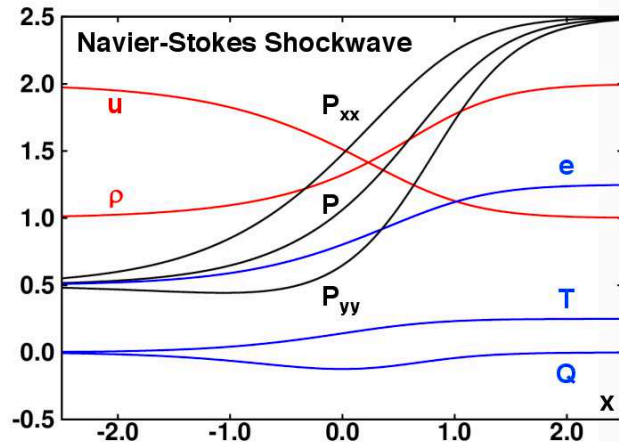


FIG. 19: This simplest possible shockwave picture includes Newtonian viscosity and Fourier heat conduction, as formalized in the Navier-Stokes equations. The Runge-Kutta solution of the conservation laws for stationary mass, momentum, and energy fluxes requires solving two ordinary differential equations for the velocity and temperature profiles subject to equilibrium boundary conditions satisfying the Hugoniot equation. The equilibrium mechanical and thermal equations of state, $P = \rho e = (\rho^2/2) + \rho T$, together with Newtonian shear viscosity and Fourier heat conductivity, give a stationary shockwave profile. We display the coordinate dependence of the mass density ρ and fluid velocity u , the pressure tensor P_{xx}, P_{yy} including the viscous contributions $\mp(du/dx)$, the energy per unit mass e , the temperature T , and the heat flux $Q \equiv -(dT/dx)$.

energy changes taking place in a steady shockwave it provides no indication of the equilibration mechanism(s) responsible. Viewing the shockwave compression process in a different coordinate frame, centered on the shockwave, can provide descriptions well suited to comparison with simulations and shown in considerable microscopic detail in **figure 19**.

In that figure cold fluid enters at the left and passes through the shockwave transition region to become a denser, higher-pressure, higher-temperature “shocked” fluid, which exits at the right. In the frame centered on the shockwave the flow is completely stationary, simplifying its description in terms of simple models such as the microscopic Boltzmann Equation and the macroscopic Navier-Stokes equations. The Navier-Stokes approach is the simpler of the two. A short computer program solving that model can be based on the three macroscopic conservation laws, conservation of mass, momentum, and energy. We illustrate this next.

The mass flux ρu is necessarily constant throughout the steady state. This follows from the continuity equation, $(\partial\rho/\partial t) = -\nabla \cdot (\rho u)$. The momentum flux, in addition to the comoving component P_{xx} parallel to the flow, includes the additional contribution ρu^2 due to the net flow velocity u in the coordinate frame of **figure 19**. A consequence of these two observations is that the longitudinal pressure-tensor component *within* the wave varies linearly with volume, the ‘‘Rayleigh Line’’:

$$P_{xx}(x) + (1/\rho)(\rho u)^2 = \text{constant [Momentum Flux] ,}$$

as the mass flux (ρu) is constant in the wave. It is remarkable that the highly nonequilibrium pressure-tensor component P_{xx} can be determined by a relatively simple velocity measurement.

A one-dimensional steady shockwave wave has stationary values of the mass, momentum, and energy fluxes throughout the wave :

$$\rho u, P_{xx} + \rho u^2, \rho u [e + (P_{xx}/\rho) + (u^2/2)] + Q_x .$$

P_{xx} and Q_x are the longitudinal pressure and heat flux, e is the internal energy per unit mass, and u is the stream velocity, u_s (for ‘‘shock’’) to the left of the stationary wave and $u_s - u_p$ (for ‘‘shock minus particle’’) to the right. Although the equations appear complicated they are quite easy to solve using the Runge-Kutta integrator. To do so integrate simultaneously the differential equations for (du/dx) and (dT/dx) . We illustrate the integration here for a simple example problem.

In this Navier-Stokes model of a shockwave we adopt the following constitutive relations:

$$P = \rho e = (\rho^2/2) + \rho T ; e = (\rho/2) + T ; (P_{xx} - P_{yy})/2 = -du/dx ; (P_{xx} + P_{yy})/2 = P.$$

The mass, momentum, and energy flux have the values (2, 4.5, 6). For boundary conditions (cold to the left and hot to the right) we choose:

$$u : [2 \rightarrow 1] ; \rho : [1 \rightarrow 2] ; P : [1/2 \rightarrow 5/2] ; e : [1/2 \rightarrow 5/4] ; T : [0 \rightarrow 1/4].$$

A little numerical experimentation shows that the continuum equations for the velocity and temperature :

$$\{ (du/dx) = P + \rho u^2 - 4.5 ; (dT/dx) = 2 [e + (P_{xx}/\rho) + (u^2/2)] - 6 \} ,$$

can be solved by starting at the “hot” side of the shockwave and integrating toward the “cold” side. The logic of the program is as follows. Given u and T compute ρ from the mass flux, after which the equilibrium pressure P is known, which makes it possible to compute (du/dx) from the momentum flux. The internal energy is then known making it possible to compute the temperature gradient (dT/dx) from the energy flux. This process provides the internal structure of the shockwave shown in **figure 19**. In the case shown in the figure the density doubles and the longitudinal pressure exceeds the transverse by about a factor of three at the center of the wave. Although twofold compression may seem extreme typical shockwave experiments carried out in laboratory settings compress metals as much as fourfold at pressures comparable to that at the center of the earth, a few million times normal atmospheric pressures.

F. Remarks on Microscopic Shockwave Simulations

Microscopic simulations have revealed two flaws in this Navier-Stokes model: [1] the nonequilibrium dependence of energy on density and temperature in the shock necessarily deviates from the equilibrium value; [2] the temperature itself within the shock is necessarily anisotropic. The kinetic temperature in atomistic simulations of shockwaves¹⁵ is easy to measure and is typically anisotropic, where the longitudinal and transverse temperatures are proportional to $\langle p_x^2 \rangle \neq \langle p_y^2 \rangle$. These two kinetic temperatures can be different within the shock by a factor of two or more in shockwaves of moderate strength. A well-documented example is the 400 kilobar shockwave model of argon, twofold compressed from the liquid¹⁵. The characterization of deviations from the linear-transport Navier-Stokes assumptions is an active and rewarding research area, well suited to microscopic modelling.

By 1973 Ashurst had developed techniques for controlling boundary regions’ velocities and kinetic temperatures through time-reversible constraint forces. His viscosity and conductivity results agreed well with the somewhat more cumbersome equilibrium Green-Kubo simulations^{6,47}. By 1980 several molecular dynamics simulations of shockwaves, with as many as 4800 particles, had been carried out, making it possible to compare the microscopic and macroscopic shockwave profiles^{15,44}. This work was particularly welcomed by those who interpreted laboratory measurements of shockwave and particle velocities to obtain equations of state for real materials. The findings from atomistic computer simulations that

strong shockwave thicknesses are only a few particle diameters, and later, that nonplanar sinusoidal-shaped shocks promptly become planar³⁶, confirm the accuracy of the assumptions underlying the Rankine-Hugoniot equation and the equations of state obtained from it through laboratory velocity measurements.

G. Three Routes to the Information Dimension for the N2 and N3 Maps

Let us complete our view of interesting computational models by turning to deterministic “maps”, the simplest models of nonequilibrium systems. In maps discrete jumps in a model phase space, usually two-dimensional, replace the continuous flows generated by ordinary differential equations. Flows require at least three dimensions plus nonlinearity for chaos. With maps linearity and just two dimensions are enough. Chaos and fractal structures can be achieved with simple linear mappings^{29,45} in a two-dimensional space.

Hopf introduced the Baker Map in 1937. Its action is reminiscent of dividing a clump of bread dough in half, merging the pieces and then repeating the division and merging *ad infinitum*. Bill Vance pointed out to Bill that a 45-degree rotation of that Baker Map serves to make it time-reversible. Adding twofold changes in area to the 45-degree rotation to the Baker Map produces the leftmost N2 map of **figure 20** and the resulting excellent fractal shown at the left in **figure 22** with its early two-iteration stage shown in **figure 21**. Maps like N2 are time-reversible and compressible, thus sharing the main features of chaotic dissipative flows based on time-reversible versions or variations of classical mechanics.

Time-reversibility of a map is analogous to the time-reversibility of Hamiltonian motion equations. It implies that the inverse map $N2^{-1}$ is identical to carrying out a sequence of three mappings, $T*N2*T$, where the time-reversal mapping $T(q, \pm p) \rightarrow (q, \mp p)$ just changes the sign of the “momentum variable” p . The reader can verify that the similar N3 map is not time-reversible.

The N2 and N3 mappings shown in **figure 20** both map the southeastern two thirds of the (q, p) domain into the southwestern one third and the northwestern third into the northeastern two thirds. We began the study of N2 in 1998³⁸ and have recently considered it in more detail³⁹. We found that three different routes to the information dimension of the N2 fractal give at least three different results! To shed light on this puzzle we developed and investigated the closely-related N3 map, for which all three routes agree.

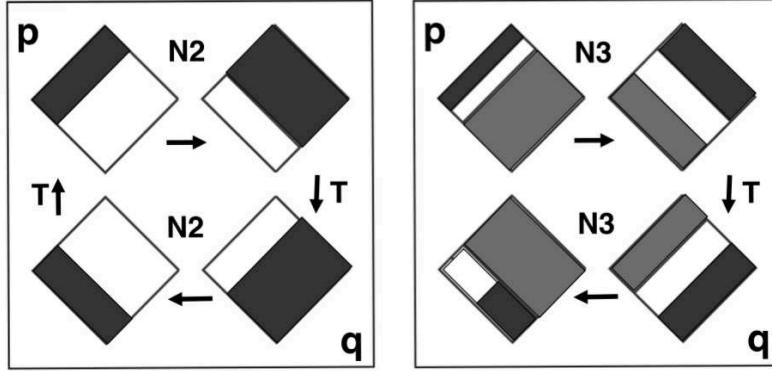


FIG. 20: The time-reversible compressible Baker Map N2 and the irreversible Baker Map N3. Both maps provide the same distributions of probability, in the fractal $q = p$ direction, after any finite number of iterations. Nevertheless the fractal sets of points generated by these maps exhibit different information dimensions D_I .

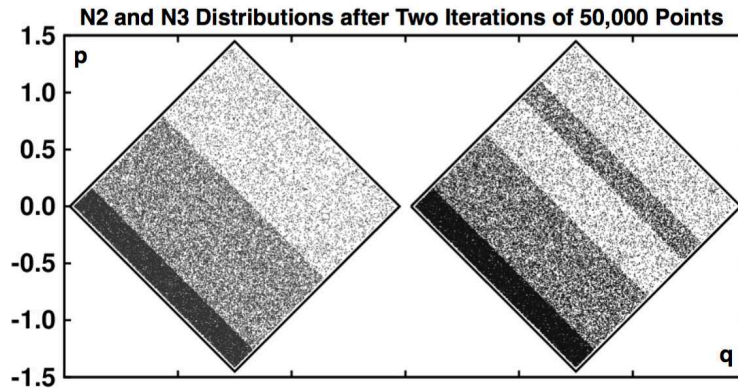


FIG. 21: After two forward mappings of N2 and N3 the distributions of 50,000 random initial points occupy nine strips of equal width parallel to the $q = p$ direction. The relative densities of the strips are 4 for the densest strip, 1 for four of intermediate density, and $1/4$ for the four least-dense strips. Both have equal information dimensions, 1.7897 overall and 0.7897 in the fractal direction. See reference 38 for additional details.

The N2 map has a straightforward linear form:

```

if(q-p.lt.-4*d) qnew = + (11/ 6)*q - ( 7/ 6)*p + 14*d
if(q-p.lt.-4*d) pnew = - ( 7/ 6)*q + (11/ 6)*p - 10*d
if(q-p.ge.-4*d) qnew = + (11/12)*q - ( 7/12)*p - 7*d
if(q-p.ge.-4*d) pnew = - ( 7/12)*q + (11/12)*p - 1*d
[Reversible Nonequilibrium N2 Map use d = sqrt(1/72)]

```

and its inverse mapping is no more complicated than the forward mapping:

```

if(q+p.lt.-4*d) qnew = + (11/ 6)*q + ( 7/ 6)*p + 14*d
if(q+p.lt.-4*d) pnew = + ( 7/ 6)*q + (11/ 6)*p + 10*d
if(q+p.ge.-4*d) qnew = + (11/12)*q + ( 7/12)*p - 7*d
if(q+p.ge.-4*d) pnew = + ( 7/12)*q + (11/12)*p + 1*d
[Inversion of Reversible Nonequilibrium Baker Map N2]

```

The details of the somewhat more complicated N3 map and its inverse can be found in reference 39.

In 1998 we adopted the conventional wisdom that the information dimension of the fractal generated by N2 was correctly given in terms of the maps' Lyapunov exponents by the Kaplan-Yorke conjecture⁴²,

$$D_I \stackrel{?}{=} D_{KY} = 1 - (\lambda_1/\lambda_2) \text{ [Kaplan - Yorke] .}$$

Kaplan and Yorke interpolated between the growth rate of a one-dimensional length, λ_1 , and the decay rate of a two-dimensional area, $\lambda_1 + \lambda_2$, to estimate the information dimension D_I of a “typical” two-dimensional map. In the N2 case the stretching direction provides Lyapunov exponent λ_1 and the shrinking fractal direction parallel to $q = p$ gives λ_2 :

$$\lambda_1 = (2/3) \ln(3/2) + (1/3) \ln(3) = (1/3) \ln(27/4) ;$$

$$\lambda_2 = (2/3) \ln(1/3) + (1/3) \ln(2/3) = (1/3) \ln(2/27) \text{ [N2 Exponents] .}$$

Together these give $D_{KY} = 1 + 0.636514/0.867563 = 1.7337$ for the two-dimensional N2 map, with the fractal direction's information dimension accounting for the 0.7337.

Another estimate for the information dimension comes from noting that each iteration of the map provides new “information” on a threefold smaller scale, with each region of constant probability “prob” giving a new region with $(2/3)\text{prob}$ and two regions with $(1/6)\text{prob}$ each for a gain in information $(2/3) \ln(3/2) + (1/3) \ln(6) = 0.270310 + 0.597253$ corresponding to an information dimension of 0.7897 rather than 0.7337. A third and a fourth estimate come from iterating a point, rather than regions, as many as a trillion times, and computing the dependence of $\langle \ln(\text{prob}) \rangle$ on the bin size δ . Using inverse powers of 3 gives an estimate of the fractal dimension 0.741 while inverse powers of 4 and 5 appear to be consistent with the Kaplan-Yorke estimate 0.7337. This inflationary wealth of estimates led us to consider the N3 map shown at the right in **figure 20**. **figure 22** shows the fractals which result from the two mappings by iterating 100,000 times, starting from the central point $(q, p) = (0, 0)$.

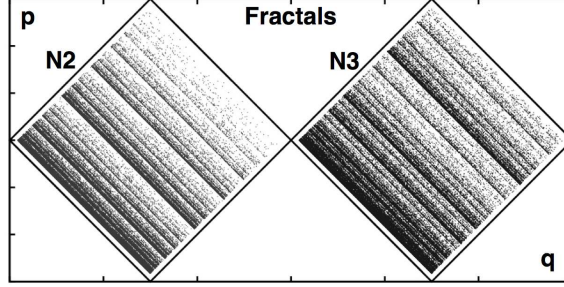


FIG. 22: Fractals generated with 100,000 iterations of the N2 and N3 maps beginning at the central point $(q, p) = (0, 0)$. The information dimension estimates for the N3 map, using a variety of meshes are all consistent with the Kaplan-Yorke prediction as well as the estimate 0.7897 based on the mapping of regions rather than points. For the time-reversible N2 map all of these estimates differ! See reference 38. Throughout this discussion the “bin size” δ is defined relative to a 1×1 unit square rather than to a 2×2 area-4 diamond.

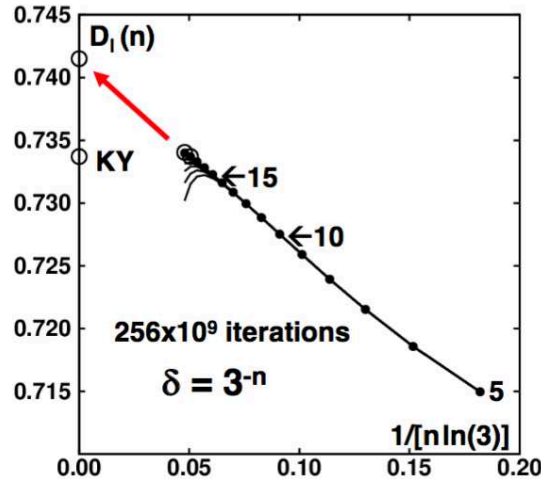


FIG. 23: Dependence of the apparent information dimension for the Compressible Baker Map N2 on the bin size δ . A straight-line extrapolation from simulations with trillions of iterations suggests an extrapolated information dimensionality of 0.741, considerably higher than the Kaplan-Yorke estimate from the Lyapunov exponents.

The N3 mapping was developed in an effort better to understand the information-dimension problems. Though not time-reversible, N3 provides exactly the same set of bin probabilities as does N2 if both start with the same uniform density. In the N3 case the Lyapunov exponents are

$$\lambda_1 = (2/3) \ln(3/2) + (1/3) \ln(6) = (1/3) \ln(27/2) ;$$

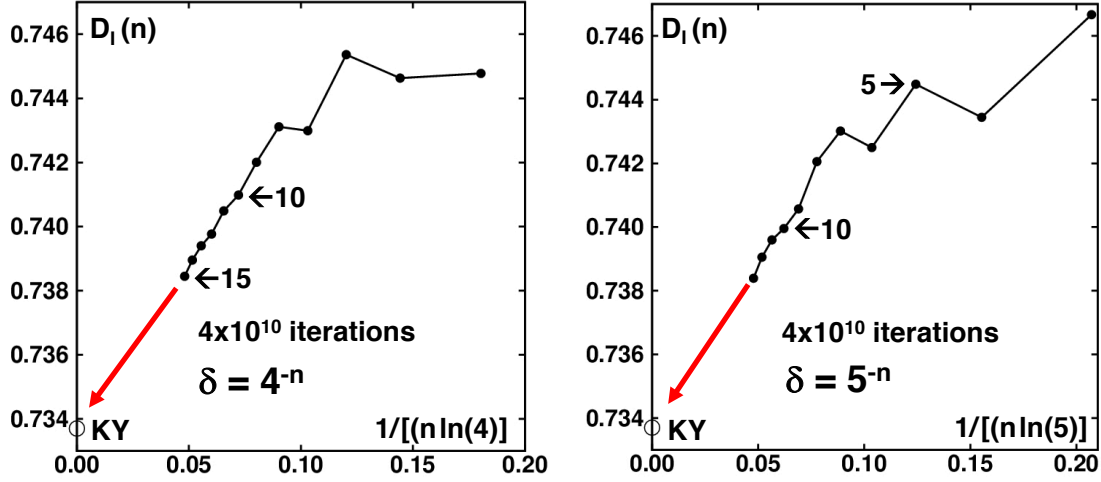


FIG. 24: Apparent information dimensions in the fractal direction for the Compressible Baker Map N2. Here series of bin sizes δ varying as inverse powers of 4 and 5 suggest good agreement with the Kaplan-Yorke estimate of $D_{KY} = 0.7337$.

$$\lambda_2 = (2/3) \ln(1/3) + (1/3) \ln(1/3) = (1/3) \ln(1/27) \text{ [N3 Exponents] } .$$

The Kaplan-Yorke prediction of the information dimension in the fractal direction, 0.7897, agrees precisely with the region-mapping dimension shared by both maps.

Mapping a set of one million points arranged originally in a uniform grid is a convenient way to carry out region mapping. **Figure 25** compares the result of applying the N2 and N3 mapping to an initially uniform grid of points. We choose a mesh $\delta = (1/3)^5 = 1/243$ and observe that five iterations of the maps produce exactly the same information dimensions for both maps, as would be expected because their region mapping probabilities are identical. However iterations beyond the fifth show that N3's dimensionality is unchanged at 0.7897 while the N2 dimensionality converges to 0.715, corresponding to the rightmost point in **figure 23**.

In sum, the N3 map shows good agreement among all four methods of estimating the information dimension, Kaplan-Yorke, region mapping, and point mapping with different values of δ , suggesting that information dimension is well understood for maps. N2 suggests the opposite and demonstrates that the reinvestigation of known problems with the ever-increasing computational capabilities described by Moore's Law reveals new problems in old areas as well as access to completely new research areas. Maps, though simple, reveal the need for yet more investigation.

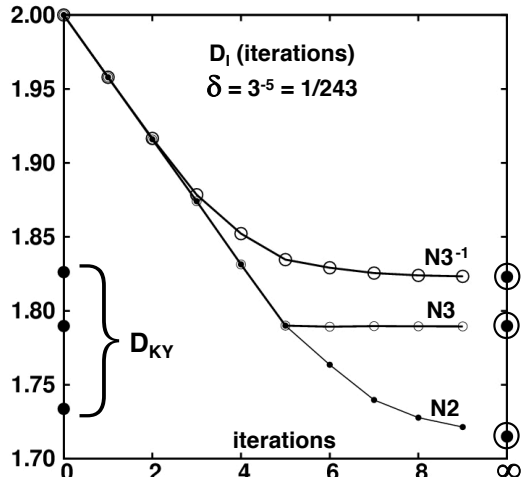


FIG. 25: Information dimensions for N2, N3, and N3⁻¹ using 243 one-dimensional bins as functions of the number of map iterations. We begin with a uniform distribution of one million points in the diamond-shaped domain. D_I remains the same for N2 and N3 through five iterations, after which their information dimensions differ. The limiting values are circled. Further mesh refinements with more bins extend the agreement but in the end the convergence remains nonuniform. The Kaplan-Yorke conjectured dimensions are shown at the left and imply that N3 and its inverse both obey that conjecture. N2 may well not and furnishes an interesting example of nonuniform convergence.

V. 60 YEARS' EXPERIENCE WITH COMPUTER SIMULATIONS

Starting out with Kirkwood's formal 1960 approach to statistical mechanics and ending up with the inexpensive trillion-timestep laptop simulations of 2020 provides a rear-view-mirror look at the effects of the computational revolution on statistical mechanics. Hours of laborious algebra and calculus have been replaced with the need to generate, process, and understand terabytes of data. Simulation has largely replaced theory as a means of "understanding". Simulations differ from ideas. For relevance and acceptance they must be reproducible. The need for reproducibility and cross-checking of conclusions is particularly important today when the public understanding of "science" has been politicized by worldwide crises, both real and imagined.

We have found that simple models capturing and detailing some aspect of reality are reliable means of organizing, understanding, and educating. The Mayers' virial series has led to sophisticated equation-of-state modelling. Molecular Dynamics has led from the three-body problem to simulations with trillions of degrees of freedom. Though the research

frontier is constantly on the move it remains as tantalizing as ever despite the changing landscapes and the ever-improving tools that we have for its exploration.

In view of the ongoing explosion of new data, results, and conjectures, fully spanning the range from useful to useless, simple models (but not too simple) continue to provide stimulating clues to progress in understanding, our goal through 60 years of joint explorations.

VI. DATA AVAILABILITY STATEMENT

The data that support the findings of this study are available from the corresponding author upon reasonable request.

-
- ¹ B. J. Alder and T. E. Wainwright, “Phase Transition for a Hard Sphere System”, *Journal of Chemical Physics* **27**, 1208-1209 (1957).
- ² B. J. Alder and T. E. Wainwright, “Molecular Motions”, *Scientific American* **201**, 113-126 (1959).
- ³ B. J. Alder, W. G. Hoover, and T. E. Wainwright, “Cooperative Motion of Hard Disks Leading to Melting”, *Physical Review Letters* **11**, 241-243 (1963).
- ⁴ B. J. Alder, W. G. Hoover, and D. A. Young, “Studies in Molecular Dynamics. V. High-Density Equation of State and Entropy for Hard Disks and Spheres”, *Journal of Chemical Physics* **49**, 3688-3696 (1968).
- ⁵ B. J. Alder, “Concluding Remarks: The Long-Time Tails Story”, pages 425-430 in *Microscopic Simulations of Complex Hydrodynamic Phenomena*, M. Mareschal and B. L. Holian, Editors (NATO ASI Series **292**, Plenum, New York, 1992).
- ⁶ W. T. Ashurst and W. G. Hoover, “Dense Fluid Shear Viscosity and Thermal Conductivity”, *AIChE Journal* **21**, 410-411 (1975).
- ⁷ G. Benettin, L. Galgani, A. Giorgilli, and J. M. Strelcyn, “Lyapunov Characteristic Exponents for Smooth Dynamical Systems and for Hamiltonian Systems; A Method for Computing All of Them”, *Meccanica* **15**, 21-30 (1980).
- ⁸ A. Bulgac and D. Kusnezov, “Canonical Ensemble Averages from Pseudomicrocanonical Dynamics”, *Physical Review A* **42**, 5045-5048 (1990).
- ⁹ N. Clisby and B. M. McCoy, “Ninth and Tenth Order Virial Coefficients for Hard Spheres in D Dimensions”, *Journal of Statistical Physics* **122**, 15-57 (2006).
- ¹⁰ C. P. Dettmann and G. P. Morriss, “Hamiltonian Reformulation and Pairing of Lyapunov Exponents for Nosé-Hoover Dynamics”, *Physical Review E* **55**, 3693-3696 (1997).
- ¹¹ M. Engel, J. A. Anderson, S. C. Glotzer, M. Isobe, E. P. Bernard, W. Krauth, “Hard-Disk Equation of State: First-Order Liquid-Hexatic Transition in Two Dimensions with Three Simulation Methods”, *Physical Review E* **87**, 042134 (2013).
- ¹² D. J. Evans, “Homogeneous NEMD Algorithm for Thermal Conductivity—Application of Non-canonical Linear Response Theory”, *Physics Letters A* **91**, 457-460 (1982).
- ¹³ D. J. Evans, W. G. Hoover, B. H. Failor, B. Moran, and A. J. C. Ladd, “Nonequilibrium

- Molecular Dynamics *via* Gauss' Principle of Least Constraint", *Physical Review A* **28**, 1016-1021 (1983).
- ¹⁴ M. J. Gillan and M. Dixon, "The Calculation of Thermal Conductivities by Perturbed Molecular Dynamics Simulation", *Journal of Physics C:Solid State Physics* **16**, 869-878 (1983).
- ¹⁵ B. L. Holian, W. G. Hoover, B. Moran, and G. K. Straub, "Shockwave Structure *via* Nonequilibrium Molecular Dynamics and Navier-Stokes Continuum Mechanics", *Physical Review A* **22**, 2798-2808 (1980).
- ¹⁶ B. L. Holian, W. G. Hoover, and H. A. Posch, "Resolution of Loschmidt's Paradox: The Origin of Irreversible Behavior in Reversible Atomistic Dynamics", *Physical Review Letters* **59**, 10-13 (1987).
- ¹⁷ B. L. Holian, A. J. De Groot, W. G. Hoover, and C. G. Hoover, "Time-Reversible Equilibrium and Nonequilibrium Isothermal-Isobaric Simulations with Centered-Difference Størmer Algorithms", *Physical Review A* **41**, 4552-4553(R) (1990).
- ¹⁸ W. G. Hoover and A. G. De Rocco, "Sixth and Seventh Virial Coefficients for the Parallel Hard-Cube Model", *Journal of Chemical Physics* **36**, 3141-3162 (1962).
- ¹⁹ W. G. Hoover, "High-Density Equation of State for Hard Parallel Squares and Cubes", *Journal of Chemical Physics* **40**, 937-938 (1964).
- ²⁰ W. G. Hoover and F. H. Ree, "Melting Transition and Communal Entropy for Hard Spheres", *Journal of Chemical Physics* **49**, 3609-3617 (1968).
- ²¹ W. G. Hoover, N. E. Hoover, and K. Hanson, "Exact Hard-Disk Free Volumes", *Journal of Chemical Physics* **70**, 1837-1844 (1979).
- ²² W. G. Hoover, "Structure of a Shockwave Front in a Liquid", *Physical Review Letters* **42**, 1531-1534 (1979).
- ²³ W. G. Hoover, "Computer Simulation of Manybody Dynamics", *Physics Today* **37**(1), 44-50 (1984).
- ²⁴ W. G. Hoover, "Canonical Dynamics: Equilibrium Phase-Space Distributions", *Physical Review A* **31**, 1695-1697 (1985).
- ²⁵ W. G. Hoover, *Computational Statistical Mechanics*, page 272 (Elsevier, New York, 1991).
- ²⁶ W. G. Hoover, H. A. Posch, B. L. Holian, M. J. Gillan, M. Mareschal, and C. Massobrio "Dissipative Irreversibility from Nosé's Reversible Mechanics", *Molecular Simulation* **1**, 79-86 (1987).

- ²⁷ W. G. Hoover, H. A. Posch and S. Bestiale, “Dense-Fluid Lyapunov Spectra *via* Constrained Molecular Dynamics”, *Journal of Chemical Physics* **87**, 6665-6669 (1987).
- ²⁸ W. G. Hoover and B. L. Holian, “Kinetic Moments Method for the Canonical Ensemble Distribution”, *Physics Letters A* **211**, 253-257 (1996).
- ²⁹ W. G. Hoover and H. A. Posch, “Chaos and Irreversibility in Simple Model Systems”, *Chaos* **8**, 366-373 (1998).
- ³⁰ Wm. G. Hoover, H. A. Posch, K. Aoki, and D. Kusnezov, “Remarks on NonHamiltonian Statistical Mechanics: Lyapunov Exponents and Phase-Space Dimensionality Loss”, *Europhysics Letters* **60**, 337-341 (2002).
- ³¹ W. G. Hoover, K. Aoki, C. G. Hoover, and S. V. De Groot, “Time-Reversible Deterministic Thermostats”, *Physica D*, **187**, 253-267 (2004).
- ³² W. G. Hoover, C. G. Hoover, and M. N. Bannerman, “Single-Speed Molecular Dynamics of Hard Parallel Squares and Cubes”, *Journal of Statistical Physics* **136**, 715-732 (2009).
- ³³ W. G. Hoover and C. G. Hoover, “Why Instantaneous Values of the ‘Covariant’ Lyapunov Exponents Depend upon the Chosen State-Space Scale”, *Computational Methods in Science and Technology* **20**, 5-8 (2014).
- ³⁴ W. G. Hoover and C. G. Hoover, “Comparison of Very Smooth Cell-Model Trajectories Using Five Symplectic and Two Runge-Kutta Integrators”, *Computational Methods in Science and Technology* **21**, 109-116 (2015).
- ³⁵ W. G. Hoover and C. G. Hoover, “Ergodicity of the Martyna-Klein-Tuckerman Thermostat and the 2014 Ian Snook Prize”, *Computational Methods in Science and Technology* **21**, 5-10 (2015).
- ³⁶ W. G. Hoover and C. G. Hoover, *Simulation and Control of Chaotic Nonequilibrium Systems* (World Scientific, Singapore, 2015), pages 204-205 for dimensionality loss; pages 213-215 for shock planarity.
- ³⁷ W. G. Hoover, J. C. Sprott, and C. G. Hoover, “Adaptive Runge-Kutta Integration for Stiff Systems: Comparing Nosé and Nosé-Hoover Dynamics for the Harmonic Oscillator”, *American Journal of Physics* **84**, 786-794 (2016).
- ³⁸ W. G. Hoover and C. G. Hoover, “2020 Ian Snook Prize Problem: Three Routes to the Information Dimensions for One-Dimensional Stochastic Random Walks and Their Equivalent Two-Dimensional Baker Maps”, *Computational Methods in Science and Technology* **25**, 153-159 (2019).

- ³⁹ W. G. Hoover, “Compressible Baker Maps and Their Inverses. A Memoir for Francis Hayin Ree [1936-2020]”, *Computational Methods in Science and Technology* **26**, 5-13 (2020).
- ⁴⁰ M. Isobe and W. Krauth, “Hard-Sphere Melting and Crystallization with Event-Chain Monte Carlo”, *Journal of Chemical Physics* **143**, 084509 (2015).
- ⁴¹ I. Johnson and A. K. Henrich, *An Interactive Introduction to Knot Theory* (Dover, Mineola New York, 2017).
- ⁴² J. Kaplan and J. Yorke, “Chaotic Behavior of Multidimensional Difference Equations”, pages 204-207 in *Functional Differential Equations and the Approximation of Fixed Points*, H. O. Peitgen and H. O. Walther, editors (Springer, Berlin, 1979).
- ⁴³ J. G. Kirkwood, “Critique of the Free Volume Theory of the Liquid State”, *Journal of Chemical Physics* **18**, 380-382 (1950).
- ⁴⁴ V. Y. Klimenko and A. N. Dremin, “Structure of Shockwave Front in a Liquid”, in *Detonatsiya, Chernogolovka*, edited by O. N. Breusov *et alii* (Akad. Nauk, Moscow, SSSR, 1978), page 79.
- ⁴⁵ J. Kumičák, “Irreversibility in a Simple Reversible Model”, *Physical Review E* **71**, 016115 (2005).
- ⁴⁶ D. Kusnezov, A. Bulgac, and W. Bauer, “Canonical Ensembles from Chaos”, *Annals of Physics* **204**, 155-185 (1990) and **214**, 180-218 (1992).
- ⁴⁷ D. Levesque, L. Verlet, and J. K urkijarvi, “Computer ‘Experiments’ on Classical Fluids. IV. Transport Properties and Time-Correlation Functions of the Lennard-Jones Liquid Near its Triple Point”, *Physical Review A* **7**, 1690-1699 (1973).
- ⁴⁸ G. J. Martyna, M. L. Klein, and M. Tuckerman, “Nos -Hoover Chains: the Canonical Ensemble *via* Continuous Dynamics”, *Journal of Chemical Physics* **97**, 2635-2643 (1992).
- ⁴⁹ B. Moran, W. G. Hoover, and S. Bestiale, “Diffusion in a Periodic Lorentz Gas”, *Journal of Statistical Physics* **48**, 709-726 (1987).
- ⁵⁰ S. Nos , “A Unified Formulation of the Constant Temperature Molecular Dynamics Method”, *Journal of Chemical Physics* **81**, 511-519 (1984).
- ⁵¹ S. Nos , “A Molecular Dynamics Method for Simulations in the Canonical Ensemble”, *Molecular Physics* **52**, 255-268 (1984).
- ⁵² P. K. Patra and B. Bhattacharya, “Nonergodicity of the Nos -Hoover Chain Thermostat in Computationally Achievable Time”, *Physical Review E* **90**. 0433004 (2014).
- ⁵³ P. K. Patra, W. G. Hoover, and C. G. Hoover, “The Equivalence of Dissipation from Gibbs

- Entropy Production with Phase-Volume Loss in Ergodic Heat-Conducting Oscillators”, *International Journal of Bifurcation and Chaos* **26**, 1650089 (2016).
- ⁵⁴ J. K. Percus, editor, *The Manybody Problem : Proceedings of the Symposium on the Manybody Problem Held at Stevens Institute of Technology, Hoboken, New Jersey, January 28-29, 1957*.
- ⁵⁵ H. A. Posch, W. G. Hoover, and F. J. Vesely, “Canonical Dynamics of the Nosé Oscillator: Stability, Order, and Chaos”, *Physical Review A* **33**, 4253-4265 (1986).
- ⁵⁶ H. A. Posch and W. G. Hoover, “Equilibrium and Nonequilibrium Lyapunov Spectra for Dense Fluids and Solids”, *Physical Review A* **39**, 2175-2188 (1989).
- ⁵⁷ H. A. Posch and W. G. Hoover, “Time-Reversible Dissipative Attractors in Three and Four Phase-Space Dimensions”, *Physical Review E* **55**, 6803-6810 (1997).
- ⁵⁸ H. A. Posch, “Symmetry Properties of Orthogonal and Covariant Lyapunov Vectors and Their Exponents”, *Journal of Physics A* **46**, 254006 (2013).
- ⁵⁹ F. H. Ree and W. G. Hoover, “Reformulation of the Virial Series for Classical Fluids”, *Journal of Chemical Physics* **41**, 1635-1645 (1964).
- ⁶⁰ F. H. Ree and T. Ree, “Statistical Mechanics of the Parallel Hard Squares in Canonical Ensemble”, *Journal of Chemical Physics* **56**, 5434-5444 (1972).
- ⁶¹ I. Shimada and T. Nagashima, “A Numerical Approach to Ergodic Problem of Dissipative Dynamical Systems”, *Progress of Theoretical Physics* **61**, 1605-1616 (1979)
- ⁶² J. C. Sprott, W. G. Hoover, and C. G. Hoover, “Heat Conduction, and the Lack Thereof, in Time-Reversible Dynamical Systems: Generalized Nosé-Hoover Oscillators with a Temperature Gradient”, *Physical Review E* **89**, 042914 (2014).
- ⁶³ J. C. Sprott, “Ergodicity of One-Dimensional Oscillators with a Signum Thermostat”, *Computational Methods in Science and Technology* **24**, 169-176 (2018).
- ⁶⁴ D. R. Squire and W. G. Hoover, “Monte Carlo Simulation of Vacancies in Rare-Gas Crystals”, *Journal of Chemical Physics* **50**, 701-706 (1969).
- ⁶⁵ D. Tapias, A. Bravetti, and D. P. Sanders, “Ergodicity of One-Dimensional Systems Coupled to the Logistic Thermostat”, *Computational Methods in Science and Technology* **23**, 11-18 (2017).
- ⁶⁶ L. Tonks, “The Complete Equation of State of One, Two and Three-Dimensional Gases of Hard Elastic Spheres”, *Physical Review* **50**, 955-963 (1936).
- ⁶⁷ G. D. Venneri and W. G. Hoover, “Simple Exact Test for Well-Known Molecular Dynamics Algorithms” *Journal of Computational Physics* **73**, 468-475 (1987).

- ⁶⁸ L. Wang and X. S. Yang, “The Invariant Tori of Knot Type and the Interlinked Invariant Tori in the Nosé-Hoover System”, *The European Physical Journal B* **88**, article number 78 (2015).
- ⁶⁹ L. Wang and X. S. Yang, “The Coexistence of Invariant Tori and Topological Horseshoes in a Generalized Nosé-Hoover Oscillator”, *International Journal of Bifurcation and Chaos* **27**, 1750111 (2017).
- ⁷⁰ R. J. Wheatley, “Calculation of High-Order Virial Coefficients with Applications to Hard and Soft Spheres”, *Physical Review Letters* **110**, 200601 (2013).
- ⁷¹ R. J. Wheatley, A. J. Schultz, H. Do, N. Gokul, and D. A. Kofke, “Cluster Integrals and Virial Coefficients for Realistic Molecular Models”, *Physical Review E* **101**, 051301(R) (2020).
- ⁷² W. W. Wood and J. D. Jacobson, “Preliminary Results from a Recalculation of the Monte Carlo Equation of State of Hard Spheres”, *Journal of Chemical Physics* **27**, 1207-1208 (1957).
- ⁷³ W. W. Wood, “Monte Carlo Calculations of the Equation of State of Systems of 12 and 48 Hard Circles”, page 152 of 310 (Los Alamos Scientific Laboratory Report LA-2827, 1963).
- ⁷⁴ W. W. Wood, “A Brief History of the Use of the Metropolis Method at LANL in the 1950s”, pages 39-44 in *The Monte Carlo Method in the Physical Sciences : Celebrating the 50th Anniversary of the Metropolis Algorithm*, J. E. Gubernatis, Editor (American Institute of Physics, New York, 2004).
- ⁷⁵ C. Zhang and B. M. Pettitt, “Computation of High-Order Virial Coefficients in High-Dimensional Hard-Sphere Fluids by Mayer Sampling”, *Molecular Physics* **112**, 1427-1447 (2014).
- ⁷⁶ R. W. Zwanzig, “Virial Coefficients of ‘Parallel Square’ and ‘Parallel Cube’ Gases”, *Journal of Chemical Physics* **24**, 855-856 (1956).